Volumetric Ultrasound Localization Microscopy of the Whole Rat Brain Microvasculature

Baptiste Heiles, Arthur Chavignon, Antoine Bergel, Vincent Hingot, Hicham Serroune, David Maresca, Sophie Pezet, Mathieu Pernot, Mickael Tanter, Olivier Couture

Received 25 June 2022; revised 28 September 2022; accepted 4 October 2022. Date of publication 13 October 2022;
date of current version 7 December 2022.

Digital Object Identifier 10.1109/OJUFFC.2022.3214185

Volumetric Ultrasound Localization Microscopy of the Whole Rat Brain Microvasculature

BAPTISTE HEILES[1,2,3] (Member, IEEE), ARTHUR CHAVIGNON[1], ANTOINE BERGEL[2], VINCENT HINGOT[1,2] (Member, IEEE), HICHAM SERROUNE[2], DAVID MARESCA[3] (Member, IEEE), SOPHIE PEZET[2], MATHIEU PERNOT[2] (Member, IEEE), MICKAEL TANTER[2] (Member, IEEE), AND OLIVIER COUTURE[1] (Member, IEEE)

[1]Laboratoire d'Imagerie Biomédicale, CNRS, INSERM, Sorbonne Université,75005 Paris, France
[2]Institute Physics for Medicine, CNRS, INSERM, ESPCI Paris, PSL Research University, 75006 Paris, France
[3]Department of Imaging Physics, TU Delft, 2629 HS Delft, The Netherlands

CORRESPONDING AUTHOR: B. HEILES (baptiste.heiles@gmail.com)

This work was supported in part by the European Research Council (ERC) through the H2020 Program (ERC Cog ResolveStroke 772786) and in part by LABEX WIFI (Laboratory of Excellence ANR -10 -LABX -24) through the French Program "Investments for the Future" under Reference ANR -10 - IDEX -0001 -02 PSL. The work of Baptiste Heiles was supported by a Marie-Sklodowska-Curie Actions Fellowship from the European Research Council through the Horizon Europe Program under Agreement 101032769-MIC.

This article has supplementary downloadable material available at https://doi.org/10.1109/OJUFFC.2022.3214185, provided by the authors.

This work involved human subjects or animals in its research. Approval of all ethical and experimental procedures and protocols was granted by the Institutional and Regional Committees for Animal Care (Comité d'Ethique pour l'Expérimentation Animale No. 59 "Paris Centre et Sud" Protocole No. 2017-23), and performed in line with the European Union Directive of 2010 (2010/63/EU).

ABSTRACT Technologies to visualize whole organs across scales in vivo are essential for our understanding of biology in health and disease. To date, only post-mortem techniques achieve cellular resolution across entire organs. Here, we demonstrate in vivo volumetric ultrasound localization microscopy (ULM). We detail a universal methodological pipeline including dedicated 3D ULM, motion correction and realignment algorithms, as well as post-processing quantification of cerebral blood diameter and flow. We illustrate the power of this approach, by revealing the whole rat brain vasculature at a 14-fold improved resolution of 12 μm, and cerebral blood flows ranging from 1 to 120 mm/s. The exposed methodology and results pave the way to the investigation of in vivo vascular and hemodynamic processes across the mammalian brain in health and disease.

INDEX TERMS Ultrasound superresolution, 3D ultrasound imaging, neurovascular imaging rodent brain atlas.

I. INTRODUCTION

COMPREHENSIVE understanding of normal vascular function, along with disease diagnosis, has led to the creation of imaging modalities capable of mapping blood circulation. In humans, Computerized Tomography (CT), Magnetic Resonance Imaging (MRI), Ultrasound Doppler(1), and contrast-enhanced ultrasound (2) can map large vasculature or evaluate perfusion level in tissue non-invasively. In animal models, finer structures of large portions of the brain can be resolved at the micrometric scale using techniques such as tissue transparization (3–7), staining (8), or micro-CT(9). They often require equipment that is restricted to pre-clinical use, long acquisition times - from several hours up to several days - but most importantly the micrometric resolution is attainable only post-mortem, which precludes investigations of blood flow dynamics. Two-photon imaging in animals through small chronic window implants has imaged the vasculature down to the capillaries at sub-micrometric scales but are limited to the cortex due to light absorption(10–12). Photoacoustic microscopy (13, 14) combined with tomography approaches is capable of imaging 3D organs in vivo, however, depth of imaging is related to its lateral resolution and so the penetration-resolution trade-off remains.

The combined use of clinically approved ultrasound contrast agents, namely microbubbles, with high frame rate echographs allows us to surpass conventional wavelength-bound resolution. These agents, which remain entirely

intravascular, are used as individual ultrasound sources - alike to fluorescent molecules in single-molecule localized optical microscopy(15)- in a technique called Ultrasound Localization Microscopy(16–18) (ULM). The echo originating from individual microbubbles can not only be localized with a resolution of a few microns (19) but can also be tracked over several tens or hundreds of milliseconds, revealing precise perfusion with high temporal sampling of various organs such as the brain (20, 21), the kidney (22), and in the context of cancer models to tumors (23–26).

However, 2D ULM implementations are inherently limited by the lack of information outside of the imaging plane. Moreover, the projection of ultrasound echoes in one plane makes flow quantification valid only for vessels contained in the plane orthogonal to the elevation direction such as in the neocortex in the brain. Plane limited 2D imaging causes projection artifacts which prevents appropriate motion correction and increases user-dependency in the choice of the plane. Finally, while imaging a single plane takes about a minute, a plane by plane approach would involve precise translation and rotation scanning, multiple injections, and prolonged imaging time considerably limiting clinical translation for 3D diagnosis of large and complex structures. The extension of ULM to 3 dimensions was originally demonstrated in an *in vitro* flow phantom representing a single sub-wavelength bifurcating vessel (9). The transition to imaging a living organ is complexified by the presence of the skull, increased number of vessels, heterogeneous microbubble speeds, tissue motion, and ultrasound-related problems such as the trade-off between Signal to Noise Ratio (SNR) and volume rate, tissue backscattering, and absorption. Several attempts have been made at 3D ULM, originally relying on using linear probes(20, 23), and then more recently using 2D matrix arrays with reduced volume rate (27). Recently published in the context of the mouse (28), 3D ULM has yet to be applied to the entire organ and needs to be equipped with proper metrics for resolution measurement, fast 3D ULM probe-independent algorithms and complemented with post-processing tools to handle large amounts of data for registration, vascular and hemodynamic characterization.

Here, we report a volumetric ULM method relying on a fully populated matrix transducer and custom-built ultrasound scanner that achieves high volume rate 3D imaging at the microscale over an entire living rodent brain. We show that the vascular physiology of the entire organ of the rat can now be characterized with precise super-resolved velocimetry thanks to in-depth optimization of ULM post-processing algorithms to handle the large amount of data produced. We measure this resolution in vivo with several metrics taken from the literature and test the robustness of the results with respect to anesthesia. Last, we introduce a clustering method to isolate trajectories into separate entities representing vessels. This adaptive segmentation method allows automated diameter measurement and easier visualization of specific structures directly from millions of microbubble paths. Thanks to these additional post-processing steps and by moving the probe over the brain we gain insight into the precise anatomical and hemodynamic characterization of the entire rodent brain vasculature.

II. METHODS

A. ANIMALS

All animals received humane care in compliance with the European Union Directive of 2010 (2010/63/EU), and the study was approved by the institutional and regional committees for animal care (Comité d'Ethique pour l'Expérimentation Animale no. 59—'Paris Centre et Sud' Protocole no. 2017-23).

8-10 weeks Sprague-Dawley rats were obtained from Janvier Labs (Le Genest-Saint-Isle, France). Animals were free from pathogens and were placed in our in-house facilities. Housed in Techniplast® cages by groups of 2 minimum and 3 when the total animal per volume ratio did not exceed values fixed by regulations, the animals were kept for at least a week before surgery. The temperature in the cages was controlled to be between 21-23°C, the humidity rate in between 40-60%. The day-night cycle was divided as follows: 7h-19h/19h-7h. Water and a commercial pelleted diet SAFE A04-10 were available ad libitum. SAFE Flake sawdust was used as bedding, enrichment such as pieces of cardboard, paper tunnels were provided and the facility vet went to visit them daily. This allowed to reduce stress during manipulation before anesthesia induction and increase the anesthesia's performance in terms of speed and robustness in time.

After 5 minutes in the induction cage filled with a mix of air and 5% of isoflurane, the animal was placed on the back on a heated plate with a respiratory mask. The mix was replaced with O_2 mixed with 4% of isoflurane. The depth of the anesthesia was tested by the absence of withdrawal reflex when pinching the toes of the hind limb. An incision was made just above the first rib in the thoracic area. The absence of movement from the animal during that incision was considered as a confirmation of the depth of the anesthesia. After the tissue was dilacerated to provide easy access to the jugular vein, two suturing strings were threaded under it. The string closer to the brain was knotted to close blood flow returning from the brain. An incision perpendicular to the direction of the vein was made and a 180 μm inner diameter polyethylene tubing (Instech/A-M Systems®) was placed inside the vein to serve as a catheter. The surgery was deemed successful when blood reflow was observed. The skin was sutured back with veterinary glue (Vetbond® 3M Animal Care Products, St-Paul, MN, USA).

The animal was then placed in a stereotactic frame equipped with a respiratory mask. The percentage of isoflurane was decreased to 3% while maintaining the absence of reflexes. 5mL of saline at 37°C was injected subcutaneously in two different doses on the left and right sides of the back of the rat to prevent dehydration. Such a procedure was repeated every 2 hours. The fur was cut off the scalp

using an animal hair trimmer to provide a clear view of the skin and a clean surgery site. The skin was cleaned first with a 4% povidone-iodine scrub solution, and second with a 10% povidone-iodine solution for additional antiseptic action (both from (Betadine®, Purdue Products, LP, Stamford, CT)). An incision was made in the scalp following a line between Bregma and Lambda points but extending from over the olfactory bulb to just behind the cerebellum (see **Supplementary figure 5 step 1, 2, 3**). The scalp was retracted and the side and the cerebellum muscles were disjoined from the skull to allow easy access to the skull. The muscles were kept away from the skull by using suturing thread. After this, the percentage of isoflurane was decreased as low as possible but above 1% to prevent lethal side-effects such as hyperventilation, cardiac deficiencies while maintaining the absence of reflexes.

A drill was used to remove a large portion of the skull to provide an ultrasound transparent window. This window was drilled using 5 different zones (see the layout on **Supplementary figure 5 step 4**). The first zone is the biggest one starting over the lambda sutures, went along the sides of the skull just below the ridges, and then joined 3 mm after the Bregma point just before the beginning of the olfactory bulb. Such a window measured approximately 12 mm in width and 15 mm in height. This window was extended to the sides and then two additional zones were drilled to provide access to the cerebellum and the olfactory bulb. The surgery took between 2 and 3 hours. A saline solution was used to keep the dura mater hydrated at all times.

B. PHYSIOLOGICAL CONSTANTS

The heartbeat, breath rate, breath distension, temperature, and SpO_2 were all monitored using MouseOx Plus pulse oximeter (Starr® Life Sciences Corporation). A decrease in SpO_2 was remedied by an increase in the O_2 fraction of the gas mix breathed by the animal. A decrease in temperature implied covering the back of the animal with a heated glove until the appropriate temperature was recovered. An increase in temperature implied lowering the temperature of the heating plate. A sudden decrease in breath rate was usually solved by lowering the percentage of isoflurane in the mix. Breath distension measurements were discarded because of a large standard deviation due to inaccuracies in the measurement device.

C. ISOFLURANE AND KETAMINE-MEDETOMIDINE ACQUISITIONS

For the anesthesia paradigm experiments, only zone 1 was removed. The surgery took in between 30 and 45 minutes. The imaging process began 30 minutes after the skull was removed. In the meantime, the brain was immersed with saline which will also serve as an ultrasound coupling medium. This allowed the physiological constants to stabilize and be less affected by surgery. We recorded these and considered them as a baseline for the rest of the experiment. Just before the interaperitoneal injection of ketamine-medetomidine (Ketamine: 87 mg/kg, Medetomidine: 50 mg/kg), isoflurane was decreased to around 0.8% and then decreased by 0.2% steps in less than one minute after the injection of ketamine-medetomidine (KM). This prevented overdosing the animal. After isoflurane was stopped completely, we waited for 60 minutes to make sure that the isoflurane completely disappeared in the blood and that its effects were null after that time. Additional time was sometimes required to make sure the physiological constants returned to the baseline. KM was injected every hour and a half after the first injection or if reflexes were observed. A half dosage was injected to prevent overdosing. This acquisition and the results exposed here come from a single animal, different from the animal where the whole brain was rendered.

D. ULTRASOUND SEQUENCE

We designed our ultrasound sequence around the computational capabilities of our system. In our case, working with RF data is mandatory for the 3D approach as the 1024 channel ultrasound scanner is unable to beamform as it is acquiring data.

A customized, programmable, 1024-channel ultrasound system [2] was used to drive a 32-by-35 matrix-array probe centered at 8 MHz with a 90% bandwidth at -6 dB, a 0.3-mm pitch, and a 0.3-mm element size (Vermon, Tours, France). The 9th, 17th, and 25th lines of that probe are not connected resulting in a 32×32 matrix array. We used that probe to transmit 2-D tilted plane waves at 9MHz frequency to increase resolution as much as possible without losing sensitivity. The probe was coupled to the brain using either water, ultrasound gel, or low concentration agar (less than 2% in water). It was placed directly over the brain with a spacing higher than 3 mm to avoid the near field. In order to map the entire brain, we place the probe in different positions with a significant overlap. The ultrasound system consists of four different Aixplorer synchronized systems (Supersonic Imagine, Aix-en-Provence, France). A combination of 12 tilted plane waves was transmitted with this order: $xz\,(^\circ) = [-3, -2, -1, 1, 2, 3, 0, 0, 0, 0, 0, 0]$; $yz\,(^\circ) = [0, 0, 0, 0, 0, 0, -3, -2, -1, 1, 2, 3]$, with x and y-directions parallel to the matrix-array probe. We increase the angles to match the maximum number of transmits allowed by the systems transfer rate without dropping the compounded volume rate below 500 Hz. The peak-negative pressure (PNP) is -294 kPa, and the ISPTA is 385 mW/cm^2. To prevent data overload and to succeed in prolonged high frame rate imaging, a specific sequence was developed with only a few milliseconds of imaging and a long pausing time: during 0.370 s, 185 compounded volumes were acquired with parameters above. The data was then transferred to Solid State Drive memory on each of the four ultrasound scanners' computers. In the first experiment (see figure 1. a), a single ULM volume is reconstructed from 540 blocks of 185 volumes in 3 minutes 33 seconds. In the second experiment, the entire brain is reconstructed form 7 times 400 blocks of 184 volumes in 17 minutes (see **Supplementary figure 6**). All the acquisitions are done at a volume rate of 500 Hz.

To provide continuous perfusion with microbubbles, 0.1 mL boli of Sonovue microbubbles prepared following the product specification sheet given by Bracco were renewed every 90 seconds, yielding a total volume injected of 1.2 mL in 18 minutes which is well below the recommended value of 5mL/kg for a single bolus recommended by the Institutional Animal Care and Use Committee (IACUC).

After acquiring all of the data, it was entirely transferred to another computer where storage has a larger capacity. This data was then processed according to the processing described below.

E. ULM PROCESSING

The ULM processing is based on the radial symmetry algorithm. The radiofrequency data is beamformed in all directions on a $\frac{\lambda}{2} \times \frac{pitch}{2} \times \frac{pitch}{2} = 80 \times 150 \times 150\ \mu m^3$ grid. The singular value decomposition is done on each of the 185 volumes [3], [4]. Of the 185 singular vectors, the first 4 are discarded and the volume is reconstructed using 181 of the lowest energy vectors. We chose the vectors by looking at the detection rate in a single acquisition and by visual evaluation of the imaging quality in 3D. To cope with lower SNR and with increased data size, we designed a new 3D localization algorithm based on the radial symmetry of the Point Spread Function (PSF). This new localization approach has been shown to retain high imaging quality while cutting processing costs by a factor as much as 50 in 2D [11]. This whole process was parallelized to keep calculation costs to four hours. The full mathematical demonstration of the radial symmetry algorithm in 3D is available in the supplementary files. The positions of the microbubbles are then converted from pixels to micrometers. The Kuhn-Munkres method for assignment problems is used to pair the microbubbles together and form tracks. This tracking algorithm is implemented on each block of acquisition separately. Tracks are interpolated by resampling the streamline on an oversampled time vector, this way saving the velocity information. Velocities are calculated using differentiation on a custom-built time vector corresponding to the interpolation of the trajectories. The results of this process are the list of non-interpolated microbubble centers, the list of trajectories with the velocities measured at each point of the trajectories.

In parallel, the beamformed data were filtered to retain only tissue signal and used for motion correction in between the different blocks. The rigid transformation calculated in that step was then applied to the corresponding trajectories block by block, allowing to correct for motion directly on sparse data rather than on each frame, thus saving computational power and time.

The whole post-processing takes place directly on the raw RF data and only the localization results are saved since it provides a much larger compression than saving intermediary beamformed data. The parallel implementation of this process takes one and a half minutes for one block if velocimetry is performed, only one minute if no velocimetry is performed, making the whole implementation for 540 blocks of 1TB run in 4 hours on a high-performance desktop computer (Intel Core i9 @ 2.9 GHz 12 cores, NVidia RTX 2080Ti, 128GB RAM @ 2133 MHz).

After processing, all trajectories were binned on voxels of size 10 μm except when resolution assessment was done where the pixel sizes are [10; 20; 40; 100; 200; 300] μm. The intensity of each voxel reflects the number of trajectories crossing this voxel. For velocity renderings, the velocity in each voxel is the time average value of the velocities of each microbubble passing through that voxel. For trajectory-based representations, the velocity at each temporal and spatial point is taken.

F. 3D WHOLE BRAIN RECONSTRUCTION

To reconstruct the whole brain we decided to perform sub-wavelength registration on 3D ULM. We rely on the contiguous volumes acquired at specific locations over the brain which present an overlap. To lower the computational cost of registering a billion-voxels sized volume, we have implemented a down sampling approach. The first volume to be stiched is the olfactory bulb to the left front hemisphere as it is the volume with the most overlap. Then we proceed from front to back and from alternating left to right, in the order that we have acquired the data. An initial transform is applied to each volume through an axis projection on the three main direction and manual rigid transformation using a custom graphical user interface. The main vascular landmarks used are the superior sagittal sinus, the inferior sagittal sinus and the main arteries of the Willis circle. Following this transform, each volume is passed to the CPU for rigid transformation using the C-elastix toobox. We relied on a three-pass Gaussian pyramid multi-resolution down-sampling of the volumes with a range [8; 4; 2] with a B-spline interpolation of the 3rd order, where we took 10,000 random new samples every time to calculate the Mattes mutual information. The optimizer was set to Adaptive Stochastic Gradient Descent and the transform was set to a Euler transform. We then applied this transformation to each volume using transformix and finally reconstructed the whole volume at once to save computation time.

G. SEGMENTATION

To characterize each vessel imaged with 3D ULM, a segmentation algorithm was used. The issue we face was that the conventional segmentation algorithm used in vascular imaging rely on continuous representation of vessels. In our case, vessels are not represented continuously but by the trajectories of microbubbles passing through them. That hinders the robustness and success of the majority of pre-filters used in intensity-based skeletonization algorithms relying on 2nd order derivatives of image intensity, which in our case is not a continuous function inside vessels. Furthermore, each volume generates around a million trajectories, a number so high that conventional algorithm based on independent streamlines (such as the ones used in Diffusion Tensor Imaging (DTI) [6] or in trajectory analysis for road control [7]) will fail to produce a result in acceptable calculation time.

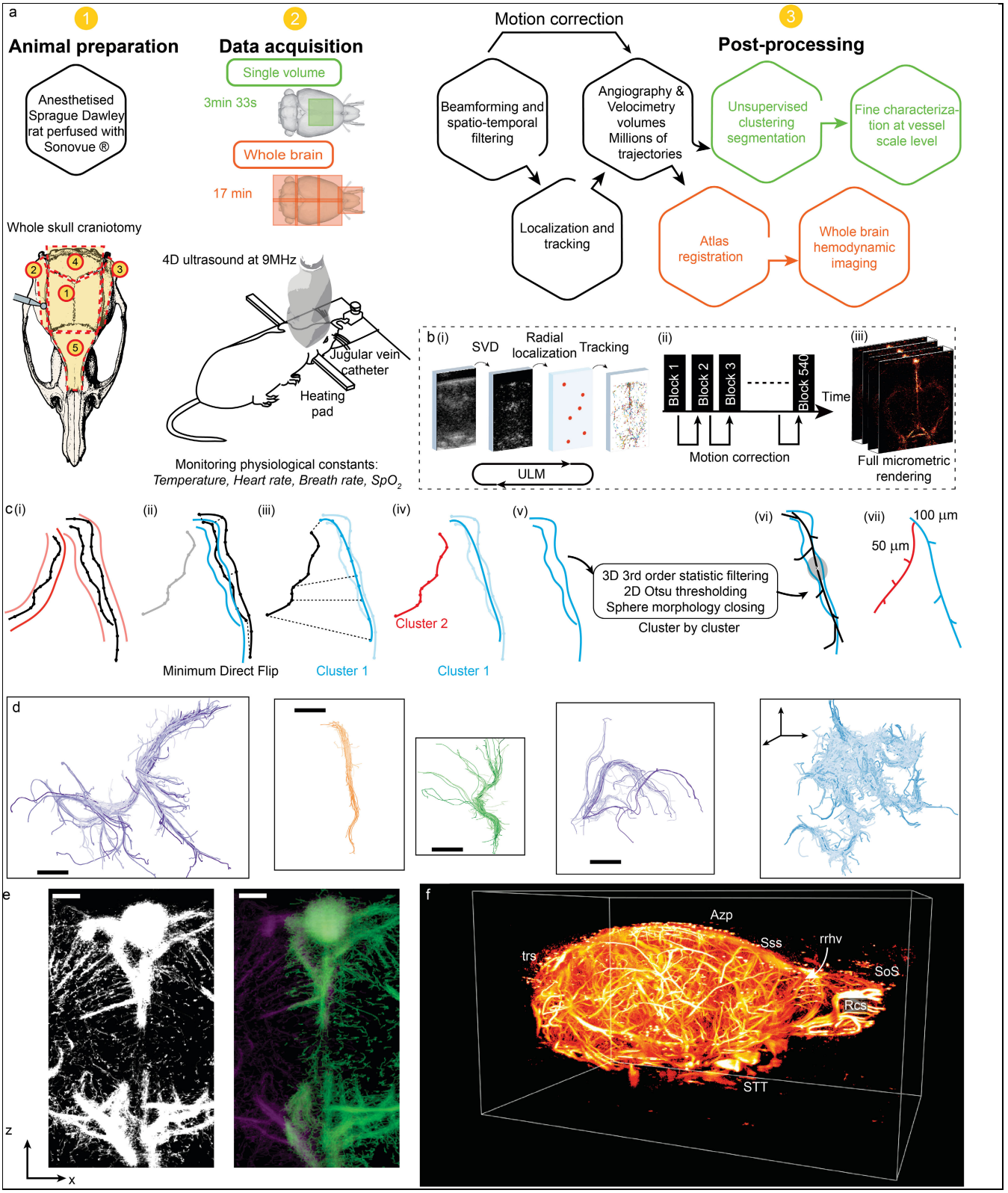

FIGURE 1. Overview of 3D ULM on the whole brain a) Presentation of the 3D *in vivo* ULM surgery, acquisition, and post-processing pipeline. The animal is anesthetized and a jugular vein catheter is placed to inject microbubbles. A cranial window is opened: for a single volume (in green in this figure), only area 1 is removed, for whole-brain imaging, the 5 windows are removed sequentially indicated by circle numbers. Data acquisition is done with 4D ultrasound at 9MHz central frequency and the animal is under constant physiological monitoring. In post-processing, the data is then beamformed, filtered, localized and trajectories are reconstructed. Post-processing steps are added for single volume (in green) to perform fine characterization at vessel level and for whole-brain imaging (in orange) to stitch volumes and register with a Waxholm space-based atlas b) 3D ULM specific processing:

i) show filtering, localization and tracking applied to all volumes acquired. ii) presents the motion correction algorithm in between noncontiguous volumes. All the volumes are acquired in a block like fashion, with a pause in between each block. A rigid transformation is calculated on tissue signal from the first volume of each block (Block 1, Block 2,...). Then this transformation is applied directly to the trajectory points. iii) the motion corrected trajectories are used to produce density or velocity maps. c) Segmentation processing illustrated on two neighboring vessels. i) The supposed borders of the vessels are drawn in red. Assuming we want to analyze 3 trajectories. ii) First, the Minimum Direct Flip distance is calculated between the two blue trajectories. As their MDF value is below threshold, they are paired and make up a new cluster defined by its centroid streamline shown in black. For any other trajectory in black, that centroid streamline will be used to calculate the MDF. iii) Second, the MDF from the other trajectory to the centroid streamline is calculated. iv) Because it is above threshold, it is used to create a new cluster. v) For each of the clusters, the velocity volume is rendered and pre-processed with 3D 3rd order statistic filtering, Otsu threshold to yield a binary image which is then morphologically closed. vi)This volume is then used for medial axis thinning skeletonization, pruned and an ellipsoid fit is used to calculated diameters vii). d)Clusters from different regions rendered from the microbubble trajectories: From left to right, 4 clusters make up an artery in the striatum (light purple), one cluster representing a cortical vessel (orange), one cluster representing the thalamoperforating artery (green) and one cluster sufficient for the rendering of the transverse hippocampal vein (purple) (scale bar 500 μm). Finally, 27 clusters render the complex vascular structure descending from the longitudinal hippocampal vein down towards the septal region in 3D. The color intensity encodes the length of the trajectories. e)Stitching of two volumes along the superior sagittal sinus: Maximum Intensity Projection on the left and Green Cyan combination on the right. (scale bar 200 μm)). f) Whole organ imaging of a Sprague-Dawley rat brain: 3D rendering showing the right part of the hemisphere. Azp: azygos pericallosal artery, ios: inferior olfactory sinus, Rcs, Rostral confluence of olfactory sinuses, rrhv: rostral rhinal vein, Sos: Superior olfactory sinus, STT: spinal trigeminal tract, trs: transverse sinus (retrogloid vein).

We decided to rely on a pre-processing step on trajectories where we regroup all trajectories in what we call clusters before implementing segmentation and skeletonization. This approach was inspired by a similar one used in DTI and fiber tracking [8]. All trajectories are first sorted by descending length. For each trajectory, the trajectory is discretized on a cubic spline curve and resampled to yield a reduced number of voxel points $N_{reduced} = 40$. Each track thus will have the same number of coordinates and the minimum direct flip (MDF) distance can be calculated. This distance is defined as the minimum of the distance between the corresponding points of two trajectories from start to end, and the distance between the corresponding points of one trajectory to the flipped version of the other. If that distance is smaller than a fixed threshold $MDF_{thresh} = 80$, then the two streamlines are paired together to form a new cluster. Should the algorithm compare all tracks sequentially, the number of operations would be $(2N)^N$. In our implementation, a trajectory is compared to existing clusters, and if the minimum MDF value from the trajectory to all clusters is below a fixed threshold, then the trajectory is added to the concerned cluster. Otherwise, a new cluster is created containing that trajectory. When a trajectory is added to a cluster, we calculate a cloud of points belonging to all trajectories in the cluster by concatenating all trajectories in a single one and discretizing it in $N_{reduced}$ coordinates. These cloud coordinates will be used to calculate the MDF value from the cluster to the trajectories, dictating whether the cluster should be updated with the trajectory or should a new cluster be created. This differs from the centroid approach used in fiber tracking where the centroid streamline is calculated for all trajectories in a cluster. The problem with the centroid method is that it is highly affected by inhomogeneities in track lengths as shown in [8]. In our case, all trajectories belonging to a vessel have different spatial lengths, depending on where they are in the vessel: longer ones are in the middle of the vessel's lumen because they belong to fast-moving microbubbles and thus travel more distance than smaller one. Smaller ones, close to the vessel's boundary belong to microbubbles which are slowed down by friction from the walls.

After clustering, for each cluster, a volume is built from the velocity measurement. Its squared intensity undergoes 3rd order statistic filtering in 3D on 26 neighbors, followed by binarization at 30% level of the Otsu threshold in 2D and morphological sphere closing of radius 3 voxels. Then, a skeleton is built via a medial axis thinning algorithm followed by branch pruning with a minimum length of 50 μm.

H. DIAMETER CALCULATION FROM ELLIPSE FITTING

For each point in the resulting skeleton, the diameter is calculated as the small axes dimension of an ellipsoid centered at this point containing all trajectories inside its volume. To do that, we rely on calculation of central moments of a region around the intensity center of mass overlaid with the skeleton center. We use Matlab to find an ellipsoid with the same normalized second central moment and we then compute an occupancy ratio defined as the number of ''on'' voxels inside the ellipse over the total number of voxels in the volume. Should this ratio be above 0.7, we increase the size of the volume around the skeleton center and compute an ellipsoid again. Once we reach the desired occupancy ratio, we take the length of the two smalles axes of the ellipse as the diameters.

I. MEASURING VELOCITY PROFILES FROM TRAJECTORIES

The trajectories in a cluster or a volume can be reconstructed on an isotropic grid with voxel size 10 μm. On this volume, 3 successive Radon transforms were applied to calculate the principal axis for rotation. Each rotation was applied to the trajectory coordinates to align them on a plane containing most of the trajectories. This allowed us to consider the main direction of flow to be straightened out in the direction $\overrightarrow{u_x}$. We could then measure diameter, flow, and speed by simply summing along specific dimensions. To do this, used flow profiles and took the first points from the center of the

profile (maximum value of velocity) that were less than 20%. Diameters were calculated along the two main dimensions, and the final diameter was taken as the average of the two, $D_0 = \frac{D_1+D_2}{2}$. For the flow, we hypothesized a fully laminar profile and took the average velocity to be $V_0 = \frac{V_{max}}{2}$. Then the flow was simply taken as $Q_0 = V_0 \pi R_1 R_2$.

J. FOURIER SHELL CORRELATION

The single ULM volume is split in half in each direction and so we have 8 sub-volumes to compute statistical significance on. The trajectories belonging to each of the 8 sub-volumes were separated into two subsets randomly. For each subset, the sub-volumes were reconstructed with each voxel having a value representing the number of interpolated trajectories passing there. The size of each voxel was 3 μm in each direction. Such a low value was chosen to be able to find the intersection between 2σ curves and the Fourier Shell Correlation (FSC) values. The Fourier transform was calculated using the fftn function in Matlab. Then, for each Fourier shell, the FSC was calculated as the correlation between the two random subsets. Unfortunately, because of RAM constraints, lower voxel values were not possible. Finally, the FSC was calculated for each spatial frequency along with the σ, 2σ, 3σ curves and plotted.

K. SATURATION

Saturation [9] can be calculated for each subset of trajectories in 3 dimensions by reconstructing volumes with different voxel sizes. We have computed that index for the single volume acquisition using the same sub-volume separation as for the FSC calculation. For each subset, we discretized the trajectories on a pre-defined voxel size matching the resolution to investigate We chose to investigate 7 different resolutions ranging from the pitch value of the probe (300 μm) to the chosen voxel size for rendering (10 μm): [10; 20; 40; 100; 200; 300] μm. A voxel is considered to be complete as soon as a trajectory has passed through it. The total number of voxel was calculated and divided by the subset volume size to yield the saturation value. The time to saturation was measured as the inverse of the tangent at the origin of the saturation curve.

L. SEPARATION MEASUREMENT

To measure the separation in the striatum, we concentrate on the branching present in that vessel. The striatum artery was segmented thanks to the clustering method. The trajectories in the cluster were reconstructed on an isotropic grid with voxel size 10 μm and 3 successive Radon transforms were applied to calculate the principal axis for rotation. Each rotation was applied to the trajectory coordinates to align them on a plane containing most of the trajectories on the x-axis. This allowed us to consider the main direction of flow to be straightened out in the direction $\overrightarrow{u_x}$. We then measured the distance between the two branching canals by slicing through the vessel orthogonally to the direction $\overrightarrow{u_x}$ using the L2-norm between the two closest trajectory points.

III. RESULTS

Several objectives were identified to overcome the challenges presented by 3D ULM such as designing a new experimental pipeline to image the whole brain, extending ULM algorithms in three dimensions and improving them to make computation times realistic while retaining image quality, and exploring the ability of the technique to quantify hemodynamic changes over the whole vasculature in 3D.

A. DEVELOPMENT OF A DEDICATED ANIMAL SURGERY AND A NEW ACQUISITION AND PROCESSING PIPELINE FOR BRAIN-WIDE IN VIVO VOLUMETRIC ULM

We implemented 3D ULM in two phases: in the first animal group, we have imaged the rat brain through a 12×12 mm cranial window in a single ULM volume anterior to Bregma (9). Then, we aimed to image the whole brain of the rat and developed a novel whole skull trepanation surgery. We thus had access to the whole brain and imaged the entire brain with volumes acquired sequentially for different probe position. We stitched these volumes together with a big-data realignment method in post-processing. The general framework of ULM is applied to both groups (outlined in black tiles in **figure 1 a)** and explained in detail in the methods section).

For hemodynamics analysis, we devised a segmentation and clustering pipeline based on trajectories rather than individual voxels (**figure 1 a)** green tiles). Thanks to this method, it was possible to visualize vessels independently by rendering their trajectories (**figure 1. c**). This allows easier navigation along the millions of trajectories and easier classification of the different vessels in the functional zones defined in the atlas. In **figure 1 d**), we have represented a few interesting structures from different regions in the brain. Depending on the size of the vessel, one cluster can represent all of it – in light purple, an artery in the striatum, orange, a single cortical vessel, in green the thalamoperforating artery – but aggregating more clusters together allows us to look at whole areas, for example, 27 clusters in blue render the vascular structure descending from the longitudinal hippocampal vein.

B. 3D IMAGING OF THE WHOLE RAT BRAIN IN VIVO BELOW THE DIFFRACTION LIMIT

To perform whole-brain imaging, we imaged 7 ULM volumes of 400 blocs over a trepanned rat at different positions mapping the whole brain (**figure 1 a**)) with an overlap of at least 200 μm. The total imaging time is 17 minutes for a dataset of 4.96 terabytes pre-beamforming. The realignment of the 7 different volumes was streamlined to the CPU processor using a rigid transformation (see **Methods**). The density and velocity volumes were then manually registered with the Waxholm Space atlas for Sprague Dawley rats [12]. A cross-section of one millimeter is shown in **figure 1 d)**. On the left, a Maximum Intensity Projection centered on the superior sagittal sinus is rendered. The stitching is not visible. For

comparison, a composed image is shown on the right with cyan and green reflecting the colors of the two volumes. The sinus and the smaller cortex vessels plunging downwards, regardless of their orientation, have a good overlap.

As seen in **figure 1 e)**, the implementation of 3D ULM results in maps of the vascular network of the rat brain. The volumetric image presented here has its voxel encoded with an intensity relating to the number of microbubbles tracks passing through that pixel. The microbubbles being intravascular contrast agents, and since the microbubble concentration is kept constant with our injection method, this intensity can be seen as an indirect measure of local blood flow. The whole-brain ULM displays the olfactory bulb with its preeminent inferior and superior olfactory sinus down to the cerebellum with its median medullary arteries [13]. The top of the cortex is split by the superior sagittal sinus into which several veins drain. On the pial surface of the brain, we can observe the different branches from the anterior, middle, and posterior cerebral arteries. Deeper structures are visible like the azygos pericallosal artery, and below the hemispheres, the spinal trigeminal tract as well as the optic nerves.

In **figure 2 a)**, we rendered a coronal slice of 1.7 *mm* of the whole brain overlaid with the Waxholm space based Atlas [12], [14], [15], [16]. The vasculature is well represented, especially in the cortex (NCx) where hundreds of arteries and veins are observable. The vessels travelling from the back of the brain through the septum (Sep) and the hippocampal region are brightly colored and clearly visible in the middle of the brain, above the thalamus (Thal-u). Most interesting is the way the pial vessels engulf the neocortex on such a large slice, forming an almost continuous border. The complex vascular tree in the striatum (Str) and fimbria of the hippocampus (fi) are visible especially on the left hemisphere. Deeper, within the midbrain, the Circle of Willis can be seen in projection as round spots. The corpus callosum (cc) exhibits a smaller density of vessels. The whole vascular brain was aligned with the Waxholm space Atlas by using regional landmarks common to the vascular and tissue structures (see **supplementary figure 7**). This enables us to segment anatomical zones and their vascular content but also to compare several organs together. These structures form the basis of a 3D vascular atlas that can be exploited to identify each part of the brain.

The velocity of each microbubble can be measured. In **figure 2 b)** we rendered the same coronal slice as panel **a)** with intensity coded to reflect the average velocity of vessels in that plane. The sign of the average velocity is computed to show upwards velocity as negative and downwards as positive. In the NCx, the number of arteries (flowing downwards) is much higher than the number of veins. The outer border formed by the pial vessels, which appeared as an almost continuous vessel in the density rendering, is also seen here and the color coding of the sign reveals that it is composed of vessels flowing in different directions.

The 1.7 *mm* density rendering for a sagittal view was rendered in **figure 2 c)** and show the brain from the olfactory bulb to the cerebellum. Focus is brought on the cerebellum (MoCb, DpCb) in the velocity rendering (**figure 2 d)**) where the veins-arteries are alternating with each other. The same is true for vessels in the brain stem where they reproduce a structure similar to what has been seen in the spinal cord [17]. The number of arteries (flowing downwards) is higher than the number of veins, which is in good agreement to what has been measured with post-mortem immunolabelling [18]. The whole volume can be explored using the supplemental visualization software packaged at https://github.com/bheiles/AtlasVis.

C. RESOLUTION MEASUREMENTS

The resolution of the technique was measured using three indices from the state of the art in the single volume experimental paradigm. The anesthesia was also changed to investigate the robustness of the resolution measurements in between volatile isoflurane (Iso) and injected Ketamin-medetomidine (KM). The approach we followed was to separate one ULM volume into 8 isotropic sub-volumes of size $5.5 \times 5.5 \times 6\ mm$ (**figure 3a**) by halving each direction once, providing statistical measurements of resolution and allowing to reconstruct volumes on finer grids without computational constraints.

The first index explored was the Fourier Shell Correlation [19], [20] a measure that computes resolution from a threshold of correlation in between independent subsets of the volume. For each of the 8 sub-volumes, the trajectories were separated in two statistically independent groups following odd-even assignment and a volume was reconstructed with a 4 μm isotropic voxel. This volume was then transformed in the Fourier domain and, the logarithmic cross-correlation coefficient over corresponding shells in Fourier space is represented for a ULM volume. The mean curve was overlaid with the standard deviation for each spatial frequency value in gray shade (**figure 3 b)**). The 2σ curve is plotted and the resolution is found as the first intersection with the cross correlation [21]. On average, the resolution was determined to be $29 \pm 17\ \mu m$ with a minimum value of 13 μm reached for one of the sub-volumes. The same was done for the same rat with a different anesthetic, the mean resolution was found to be $24 \pm 9\ \mu m$ and a minimum of 12 μm was reached, showing no statistical difference (paired t-test, $p = 0.49$, $n = 8$). The resolution measurements were calculated for motion corrected datasets (Iso Mo-co/ KM Mo-co).

A second way to measure resolution is to come back to its literal definition and consider the ability of the system to separate neighboring structures [1]. The trajectories in these arteries were reconstructed on an isotropic grid with voxel size 10 μm and the vessels were aligned with their centerline's principal axis (see Methods). The distance between the two branching canals was measured as the $L2{-}norm$ between the coordinates belonging to the two closest trajectory points from the outside borders of the canals. The minimal distance measurable in the ISO case was $17\ \mu m\ (\frac{\lambda}{10})$ (**figure 3 c)**). The same process was repeated for the KM case and the distance was found to be $12\ \mu m(\lambda/14)$.

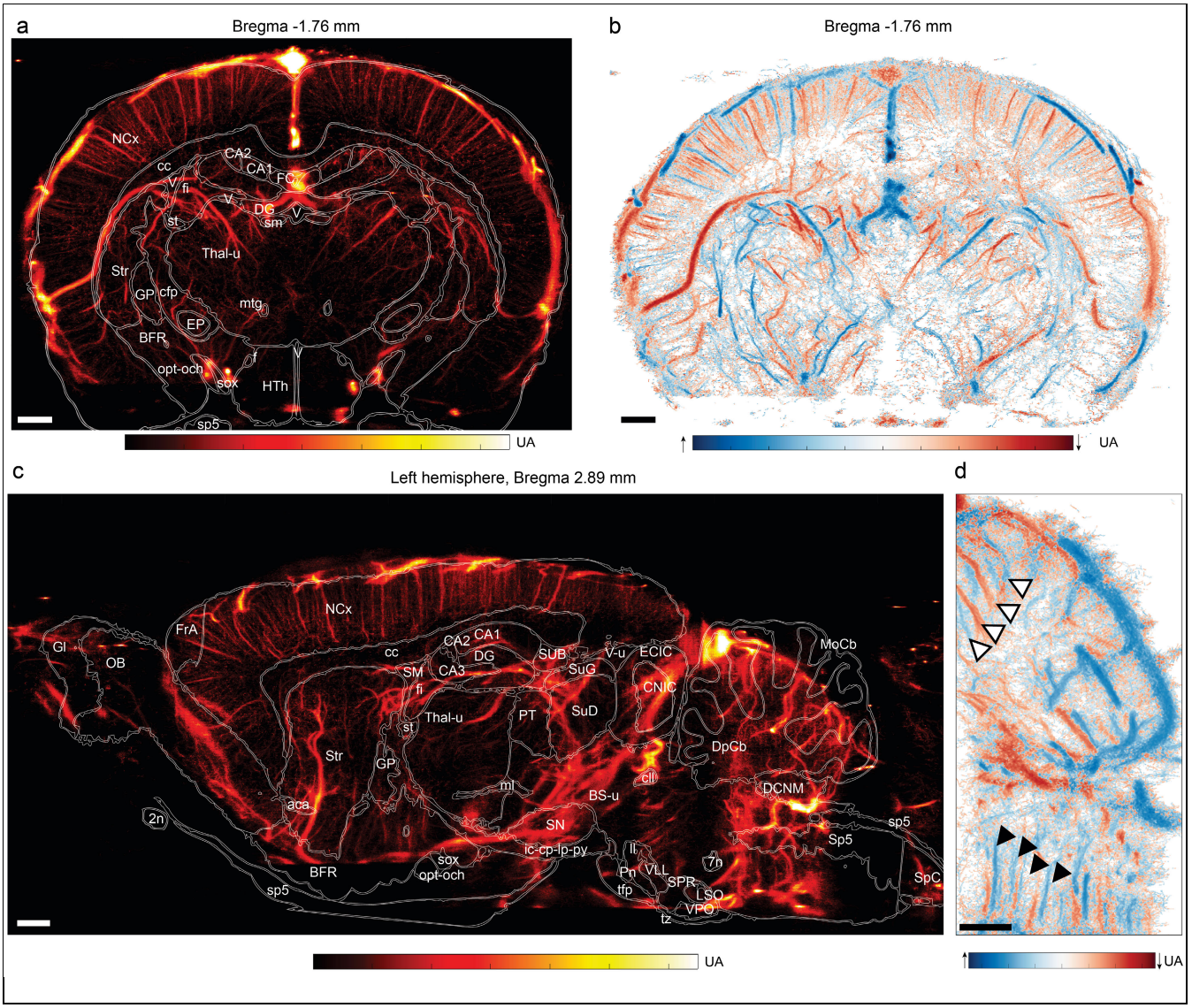

FIGURE 2. **Whole brain rendered from density and velocity measurement a) Density based rendering in coronal view overlaid with the associated Waxholm space Atlas. The position of that slice with respect to the Bregma landmark from the atlas is −1.76 *mm*. The anatomical delineation are based on image contrast from MRI data acquired on an 80 day old male Sprague Dawley rat [12], [14], [15], [16]. The abbreviations used are identical to those used in this atlas and are available in supplementary table 1. For each pixel displayed, the sum of the intensity 1.7 *mm* around the Bregma position is computed and then compressed with a square root to enhance signal from smaller vessels. The units are arbitrary. Scale bar is 1 *mm* across, and pixel size is isotropic. b) Average velocity based rendering in coronal view. The average value of non-zero velocities is computed for each pixel around a 1.7 *mm* slice around Bregma position −1.76 *mm*. This value is then L^1-normed and compressed with a cubic root to enhance the signal from smaller vessels. The sign of the original velocity is retained with the convention that negative velocities are oriented upwards and positive downwards. The units are arbitrary but reflective of the average velocity in the coronal plane intersecting a vessel. In areas where the concentration of vessels is high, the pixel value will tend to be averaged. In the neocortex (NCx indicated in panel a), the color code matches artery-vein classification as downwards-upwards/red-blue. c) Density based rendering in sagittal view with the associated Waxholm space based Atlas. The intensity displayed is calculated the same way as for panel a. Scale bar is 1 *mm* across, and pixel size is isotropic. d) Average velocity based rendering centered on the molecular cell layer and deeper layer of the cerebellum (MoCb and DpCb respectively). The intereaved structure of veins and arteries in the white matter of the cerebellar lobules is visible on the top left part of the image (white arrows). Such a structure can also be seen deeper in the brain stem (BS-u) with a regular spacing of upward/downward flow (black arrows). Scale bar is 1 *mm* across, and pixel size is isotropic.**

The 8 sub-volumes were also analyzed for their resolution with respect to saturation [9]. After being reconstructed with isotropic voxel sizes of [300, 200, 100, 40, 20, 10] μm, the saturation time was calculated and plotted as a function of pixel size. The total time of acquisition used to reconstruct this ULM volume is 3 min and 33 s and is plotted as a red dashed line (**figure 3 d**)). On average the theoretical resolution reachable for this time of acquisition is found to be

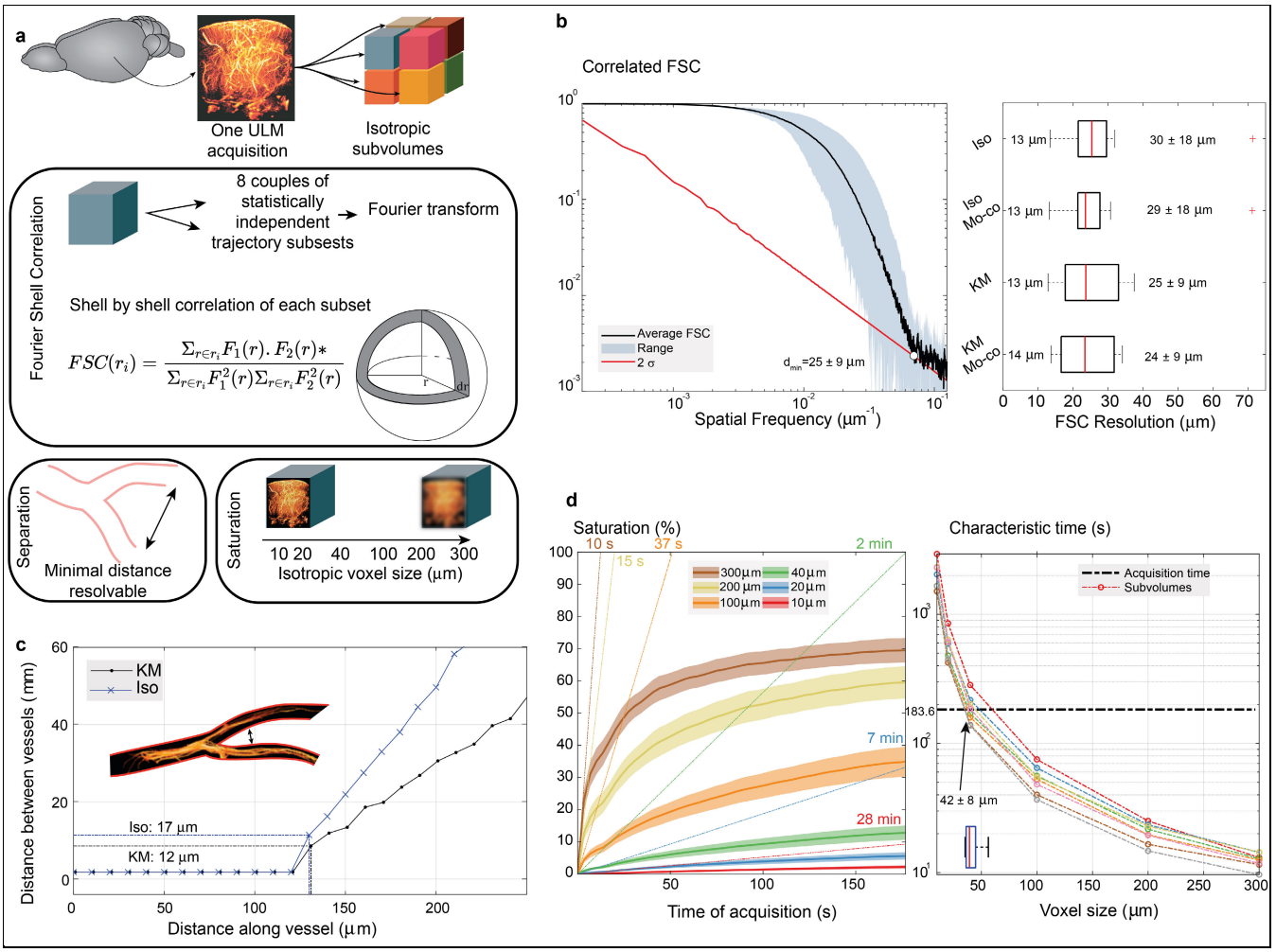

FIGURE 3. Quantifying resolution on a single ULM volume with 3 state of the art metrics a)Illustration of the three different approaches used to quantify resolution: First, a single volume ULM density rendering is divided into 8 isotropic sub-volumes. These sub-volumes will be used to calculate the resolutions b)The range of the FSC is presented in blue, overlaid with its average in solid black and the 2σ curve in red. This resolution is calculated for one ULM volume acquired under both anesthetics (Iso/KM) and with/without motion correction. Values are represented in a boxplot with whiskers indicate upper and lower quartiles. The minimum value is on the left of the boxplot while the average and standard deviation are written on the right c)Separation index: the distance between the two main branches of the striate artery clustered below is calculated, the minimum non-zero value indicates the minimum resolution attainable. This index is calculated for both anesthetics Iso and KM. d) Resolution measured with saturation: in color, saturation for different voxel sizes with respect to time is measured (average is overlaid in solid line over standard deviation in transparent curves). Next, the characteristic time calculated from saturation is plotted in function of voxel size for each of the 8 sub-volumes. The acquisition time is indicated in a dotted black line.

4 times better than the wavelength at 9 MHz, at 42 μm, with a minimum of 27 μm ($\lambda/6$). The worst-case scenario was also sub-wavelength at 75 μm. The results for the same rat with a different anesthesia are also presented and show similar results ($mean = 65\ \mu m$, $min = 32\ \mu m$, $max = 80\ \mu m$).

D. CASE STUDY: THE STRIATE ARTERIES

To showcase our ability to image deep into the brain we have chosen to illustrate a number of concepts and possibilities of ULM in a specific case. An interesting functional region is the striatum. Prone to stroke but also involved in reaching mechanisms, Parkinson's disease, and addiction [22], [23], [24], we will focus on the irrigating arteries of this region to expose hemodynamic quantification at the micrometric scale. They branch out from the middle cerebral artery (**Figure 4. a**)) in successive structures with decreasing diameters arranged in a lattice-like fashion [25].

The whole volume was clustered and we identified the anterior striate artery as a single cluster (represented with length of trajectory color in **figure 4a**), overlaid on the other clusters represented in gray). The cluster was skeletonized and the diameter of each vessel was measured at every point of the skeleton. The average diameter per segment of the skeleton is represented in **figure 4 b**). The decreasing size of the upper branch of the artery is apparent in both our measurement and the trajectory-based image. The smallest diameter measured was 22 μm while the main branch of the vessel measured 120 μm on average.

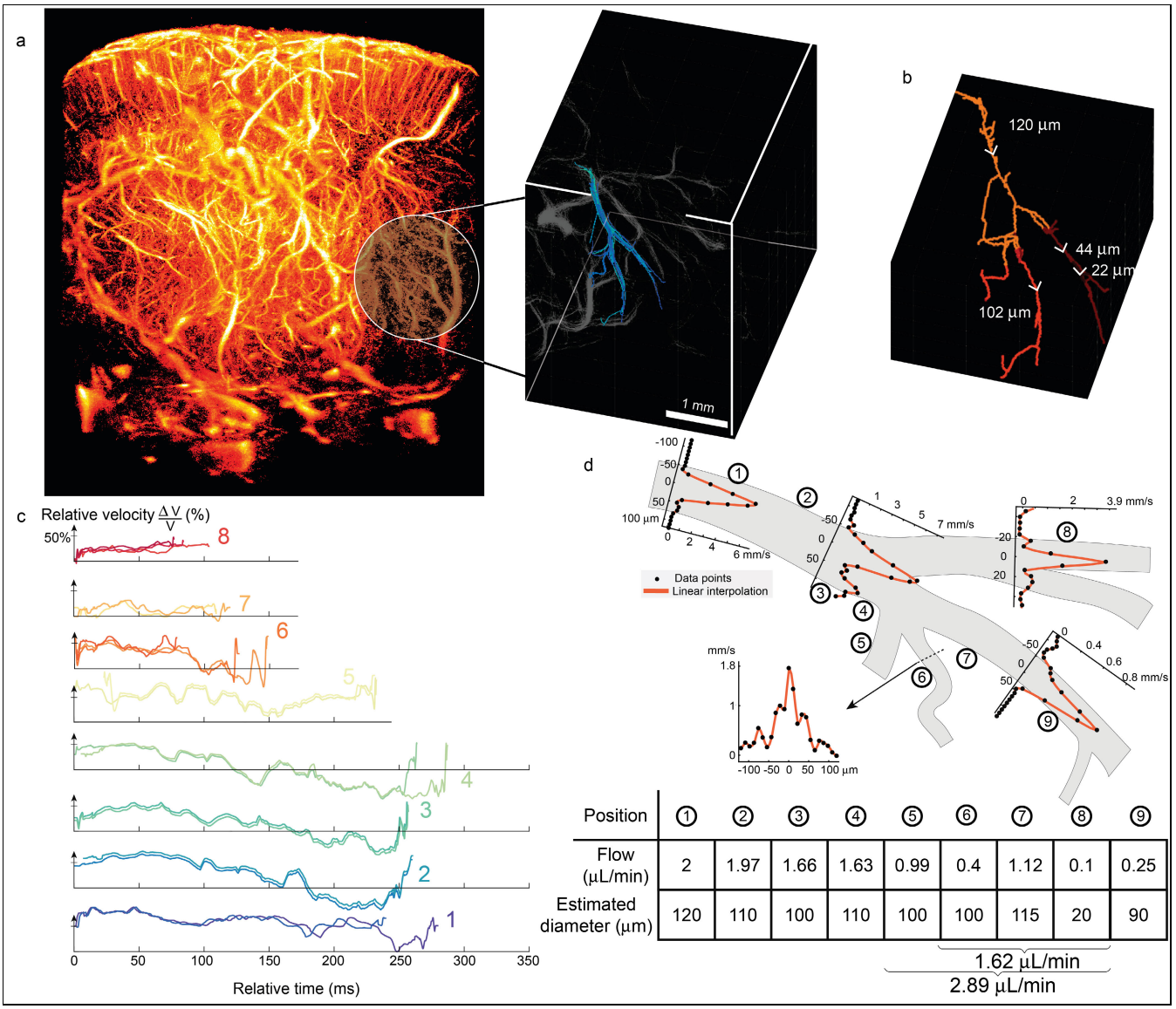

FIGURE 4. Case study: Striate arteries a) ULM volume of the rat brain from an offside coronal view: Intensity corresponds to the density of microbubbles passing through each voxel. The zoomed-in portion on the right shows trajectory-based representation. The volume presented here measures 3 x 5.5 x 7 mm^3 and is located 4 *mm* deep below the cortex surface and is reconstructed with a voxel size of 10 x 10 x 10 μm^3. The trajectories not belonging to the cluster including the striate arteries are in gray, while the ones of interest are color-coded according to the length of the trajectories. The motion was corrected in between each block with rigid transformation. b) Measurement of diameters inside the striate arteries: the diameters were calculated as the short axes' dimension of an ellipsoid fitted along the centerline containing all trajectories. The average diameter between two nodes after segmentation is indicated here with a color code. c) Velocity dynamics of microbubbles inside 17 trajectories: a few trajectories inside the striate artery have been selected and their velocity variation $\frac{\Delta V}{V} = \frac{V(t)-V_{max}}{V_{max}}$ are represented in function of time. These trajectories were grouped together based on their velocity variation over time. The velocity variation inside trajectories are representative of the pulsatile flow present in the arteries. As such, microbubbles in the same vessels and acquired during the same heartbeat exhibit the same patterns. Because of discontinuous block-to-block acquisition, some trajectories are interrupted mid-acquisition, which explains why they don't span the same time frame. d)Wall to wall flow profiles in the striate artery and flow analysis: The outer border of the realigned projected striate artery is represented in black. For 5 different positions, the flow profiles are taken as the average velocities over a 840 $\mu m \sim 5\lambda$ slab colinear to the maximum flow streamline. The velocity points are represented in solid black dots and a spline interpolation model in solid orange curve. The axes are indicated in micrometers and mm/s. Circled numbers indicate where the flows and diameters are calculated in the table.

Thanks to the high temporal sampling of ultrafast ultrasound, we can track the velocity dynamics of each microbubble trajectory. **figure 4 c)** presents plots of trajectories from individual microbubbles in function of time and color coded according to their length. The relative variation of speed was found to be as much as 94% in the longest trajectory. Pulsatile

flow is observable in most trajectories where the speed is modulated by heartbeat and packets of trajectories exhibit similar peak-to-baseline variation. The shorter the trajectories are, for example 6; 7; 8, the less they exhibit variation of velocity but their dynamics remain similar. The heartbeat of the rat during this acquisition was measured to be around 300 bpm on average, yielding a heart cycle of 0.2 s. The longest trajectory we observe here lasts for 0.28 s, which is consistent with the observation of a single pulse in the velocity dynamics.

In **figure 4d)**, we have outlined the vessel walls and superimposed the velocity profiles calculated at several points. These profiles are derived from a spatially averaged velocity calculated over 840 $\mu m(5\lambda)$ in the direction of the flow and aligned with the main axis of the vessel. The microbubble velocity in this vessel reached a maximum of 7.2 mm/s and could be as low as 1.4 mm/s. At the branching sites (3 and 4), one can see the velocity profiles getting separated upstream and exhibiting two distinct maxima in their distribution. Profiles taken a few hundreds of micrometers downstream of the bifurcation return to fully developed profiles. At each bifurcation, the profiles show the same behavior, separating in two, with higher velocity towards the main branch. We have calculated the flow assuming a Poiseuille profile and the diameter based on the profiles (see **Methods**). The total flow upstream from the branch at points 6, 7, and 8 gives us a value of 1.62 $\mu L/min$, while the original flow closest to the beginning of the branch is evaluated at 1.66 $\mu L/min$, in good agreement with conservation of flow. The values calculated with the flow are on par with the values calculated in the skeletonization.

IV. DISCUSSION

We have demonstrated 3D *in vivo* imaging of the vasculature below the diffraction limit involving an extensive rework of the animal model as well as a redesign of the post-processing techniques. The acquisition method, as well as the image formation algorithms, were changed to adapt localization and integrate motion correction schemes. Extending 2D metrics to the 3D case, we provide evidence that 3D ULM is capable of mapping structures as close as 12 μm apart, render the cerebral vascular system with a minimum FSC based resolution a tenth of the wavelength at 17 μm, and capturing hemodynamic changes deep within the living brain. Finally, by applying this imaging technique sequentially after complete skull removal, the entire brain was rendered with a 12 μm voxel grid along with blood velocities up to 120 mm/s and registered with a Waxholm based atlas. We further improved 3D ULM by introducing two new methods for trajectory-based clustering and flow analysis to provide complete vasculature analysis in a semi-automated manner. These results are packaged in a graphical user interface where the user can explore the rat vasculature and measure diameters, blood velocities and flow automatically. This enables 3D ULM to leap forward as a quantitative imaging tool for vascular applications.

Brain-wide imaging with 3D ULM, which can be applied to all organs, has the tremendous advantage of visualizing the vascular dynamics at play over a wide range of spatial scales. Sampling all microbubbles at the same time over large areas allowed to depict complex structures and to follow their trajectories regardless of the vessels' orientation, which is out of reach of current techniques. The advantage of such an accurate representation of the vessel lies in the ability to calculate diameters precisely which could then be used to propagate flow models inside each vessel. Ideally, imaging microbubbles in 3D rather than in 2D also allows reducing acquisition time per injection as all microbubbles contribute to image construction rather than just the ones in the field of view. We have calculated in **figure 3 c)** that the resolution found by calculating the saturation is on average 42 μm. This is an order of magnitude larger than what is found in 2D at an ultrasound frequency of 15 MHz (Hingot et al. [9] calculated around 5 μm for a 4 minute acquisition). For the same volume of imaging and with all other parameters kept identical, 3D ULM is thus much faster than plane by plane ULM as the insonified volume is bigger, and requires only one bolus. However, this approach postulates that all pixels should be saturated, which is not always the case regardless of the dimension. The lower resolution we obtain compared to the 2D case is to be put in perspective as the frequency of the probe is different and the 4D ultrasound scanner is an innovative design and not a commercial one. Compared to results obtained by our team on a conventional 256 channel scanner where the volume rate was limited to 247 Hz [26], the use of this specific scanner allows higher volume rates and as such enables to image fast moving organs such as the heart and reduce acquisition time. Our maximum resolution attainable is also lower than that attained in transcranial mice [27] with the same probe thanks to the complete removal of the skull and to the improved performance of the radial symmetry algorithm compared to the Gaussian Point Spread Function fitting [11]. Moreover, the radial symmetry algorithm demonstrated here in 3D does not need simulation of the ultrasound probe first such as in the method exposed in transcranial mice. Full acoustic simulation, depending on the probe and the ultrasound sequence used can be computationally demanding. Higher frequency row column addressed or sparse array probes are beginning to emerge as valid alternatives to fully addressed probes and the translation of our technique to any probe design *ad hoc* is a tremendous advantage [28], [29]. The mathematical demonstration is available in supplementary materials.

The lower sensitivity of 2D array compared to linear probes is also a potential explanation to the discrepancy between the 12 μm resolution we evaluate and the incomplete depiction of the capillary level vascular network in the images presented here. Based on our previous work in 2D where we have compared microangio-CT and 2D ULM, we should be able to depict capillaries with higher sensitivity probes [11]. Another explanation for this lack is the use of SVD filtering which relies on the spatio-temporal signature in each pixel

of tissue and microbubbles. Slow-moving tissue is highly coherent in space and time, but hematocrits or microbubbles are fast-moving and thus bear a different signature in the singular value basis. This holds largely for the main levels of the vasculature but combined with a lower SNR means that slow-moving microbubbles in capillaries might be filtered out [4]. Increase in sensitivity or the development of filter-independent detection ultrasound sequence are likely to restore our access to capillaries [30], [31]. Finally, as ULM is a cumulative technique, a longer acquisition time might also allow to depict more of the vasculature.

We have presented the methodology to measure resolution in 3D with 3 different metrics pertaining to separation of close objects, saturation and statistical differences, taken from our previous work on performance and resolution measurement in ULM (34), where their respective strengths and weaknesses are discussed. We have computed these metrics on a single acquisition volume, due to computational power constraints. For the Fourier Shell Correlation (FSC), we were already on the verge of what is possible with the computer at our disposal for the Fourier transform part. We had to develop a custom 3D FFT algorithm to circumvent memory restrictions. By computing the metrics on 8 sub-volumes within one acquisition however, we are able to provide a good statistical sample. The comparison of the different resolution criteria and their results when calculated on the same animal undergoing different types of anesthesia, vouches for the robustness of 3D ULM. The non-significance of the statistical test for the FSC based resolutions presented in **figure 3b)**, does not enable us to conclude about a potential influence of physiological condition during the recording on the final resolution of the image. Because the final images are composed of millions of trajectories taken at different times of the cardiac cycle, they tend to integrate the variation in frequency content that is brought by hemodynamic changes.

As highlighted in **figure 4**, hemodynamics changes can still be picked up in individual microbubble trajectories. This demonstrates that while ULM is a minute-long process, it is composed of individual events sampled at very high temporal resolution, giving access (though partially) to physiologically induced variations locally. The technique is thus a combination between a global approach where the organ's vascular anatomy can be represented with micrometric precision every few minutes and a local approach where the organ's hemodynamic activity is described on the millisecond timescale at sparse spatial coordinates. In a specific region in the brain, multiple trajectories can be extracted and dynamic information about cerebral blood flow can be recovered. The characterization of flow outlined in **figure 4 d)** is made possible thanks to the information of velocity and an accurate representation of the vessel in the three dimensions. However, we see that conservation of flow is not respected when we take into account vessel 5 into our calculations. Should we include vessel number 5, the increase in total flow is higher by 174% at 2.89 $\mu L/min$ instead of 1.62 $\mu L/min$. Considering the inlet flow at the position closest to the branching (labeled 3 on the image), was evaluated to be 1.66 $\mu L/min$, and the diameters measured at positions 1, 2, 3 and 4 are all in the same [100; 120] μm range, we hypothesize that vessel 5 is irrigated by another artery that we have not considered into the clustering method, or that we are missing in our ULM acquisition due to either acquisition time constraint or because the feeding vessel is too small to be picked up by our implementation of the technique. Because the clustering algorithm is sensitive to the order the trajectories are presented in [8], here it may be failing because the longest trajectories are used first to build clusters and then smaller trajectories are paired with the clusters. As such, the algorithm does not pair large vessels together but pairs smaller vessels to the larger ones. The speed of this algorithm outweighs greatly its ability to pair clusters together.

The application of our technique on the entire brain allows to visualize the cerebro-vasculature in an entirely new way. Compared to existing optical technique where acquisition time is several days and post-mortem, we offer a sub-hour acquisition time *in vivo* capable of imaging sub-wavelength phenomena at high volume-rate. In **figure 2**, we show that it is possible to combine our technique with an MRI-based atlas to identify several anatomical structures. Several interesting observations stem from this registration in terms of density of the vasculature in precise areas but also of the importance of an accurate flow visualization to discriminate vessels. In conventional 2D ULM, the inability to measure the velocity in the third dimension does not allow to separate structures flowing orthogonally to the imaging plane well which can render precise classification of vessels arduous. Several limitations appear from this registration. First, anatomical regions localized deep in the brain such as the spinal trigeminal nucleus, the optic nerves are not well observed. Other regions such as the deep part of the neocortex are clearly depicted but these regions are much more vascularized. The increase in the quality of 2D matrix array fabrication and thus of SNR of volumetric images could remedy to this issue. Second, we can see that the brain is well-fitted inside the Waxholm-space based atlas almost everywhere but the cerebellum. In our case, the cerebellum seems to sink well below the neocortex while in the atlas, it is higher up. The technique presented here was applied to a trepanned rat brain. The craniotomy surgery implemented here induces tissue-expansion which can lead to modification of the structure of the brain. As our experiment is terminal we do not see any infections during surgery and imaging and we hypothesize that similarly to what is done with smaller craniotomies [32], it would be possible to do large chronic cranial windows.

The animal model was adapted to maximize the SNR of the images and to be able to deliver the highest resolution possible. Transcranial ultrasound localization microscopy is possible [27], [33], [34], [35], but the aberration of the ultrasound waves, when it goes through the skull, results in a decreased imaging quality, especially in the rat. Interesting

algorithms to correct bone aberration have been put forward. Ideally, this study should be complemented with a MRI scan of the brain to match the atlas more precisely.

The brain was chosen to demonstrate the possibility of the technique because its motion can be limited through the use of a stereotactic frame. Our method can be applied to any organ but would require partially adequate motion compensation schemes such as the ones presented here. For larger motions, imaging quality can benefit from applying volume to volume correction rather than block by block. Thanks to ultrafast volume rates of up to 500 Hz, we were able to measure a large range of velocity up to 120 mm/s. The upper limit of this range is given by the maximum frame rate attainable and the maximum linking distance between two frames, a value set during the tracking algorithm. The lower bound of this range is about 1 mm/s, the lower limit to which the SVD filtering fails. Such a high frame rate is unattainable without the use of a dedicated ultrasound machine composed of 1024 channels and will prove useful to decrease acquisition time, correct for motion more accurately in non constrained organs such as the liver or kidney or even observe higher velocities in the coronaries in the heart.

Due to technological limitations such as the size of the acquisition data, we accumulated a number of microbubbles insufficient to characterize the capillary bed [9]. Methods to increase the number of detectable microbubbles [30] could be exploited along with compressed-sensing approaches, to drive the cost of acquisition to a minimum. Several approaches have been developed in 2D that might be of interest to 3D should they be extended. Deep learning methods to find microbubbles buried deep down in the non-filtered data should also be of interest but the cost in memory of developing these to 3D remains quite high. The time it takes to acquire the 3D ULM representation of the brain also constitutes a limitation to our technique as the physiological variations of the whole organ will not be measured at the same moment. We only possess information where microbubbles are located at a precise point in time and so can represent hemodynamic changes over limited scales. In our implementation, the heart rate, breathing rate, temperature were controlled throughout the whole experiment, and anesthesia, heating pad temperature, oxygen inflow were adapted to limit the alteration of the physiological constants.

Our probe was limited in size/number of elements and, in the case of rats, the whole-brain imaging needed realignment of several acquisitions. While the anatomical description of the organ is scarcely affected by this thanks to sub-voxel precision of the realignment, the hemodynamics are not as microbubble trajectories are cut-off in between volumes. Finally, this stitching approach has to be put in perspective to what is done in 2D optical scanning imaging techniques, where every plane needs to be registered.

The results presented here have required extensive post-processing. The steps related to localization, tracking, and filtering are relatively easy to get accustomed to, on the other hand, the clustering, segmentation, and hemodynamics processes are much more complicated and finely tuned for our application. The unsupervised fashion in which the clustering method operates already simplifies the workflow by just needing to adjust the Minimal Direct Flip value and custom thresholds on trajectory length, duration or timestamps. Because the clustering method we use first sorts the trajectories by increasing duration, we first create a basis of clusters with the underlying assumption that longer trajectories will depict vessels more accuratey than small ones. Thanks to this step we dispense of the dependence of the algorithm on cluster initialization raised in the original paper [8]. To apply our technique to other organs, adaptation of these algorithms and methods, changes might be needed, especially in tortuous vessels present in tumor environments. This method has shown its limits in DTI due to its inherent process but other methods have been applied in that field to more complex structures relying on additional pre-processing with voxel-based pre-classification [36] or multi-step clustering [37]. We foresee that other approaches for example based on machine learning-based will emerge to have a more generalized method of hemodynamic characterization, similarly to what has recently been published in the field of tissue clearing [18], [38].

Finally, the results shown here depict the anatomical and hemodynamic features of the brain but do not have access to biological or chemical markers. The use of tagged microbubbles with proteins to monitor biomarkers has been brought forward in the field of biomolecular ultrasound [39]. Development in smaller and more targeted contrast agents [40], [41], [42], [43] could extend its applications to the extravascular space. The combined use of such contrast agents will give access to biomarker mediated ultrasound super-resolution similarly to what has been shown in clearing techniques [44] and in optical superresolution [45]. The application of brain-wide ultrasound localization microscopy as a pre-imaging step for other applications such as functional ultrasound is also of great interest. *In vivo* micrometric imaging of the coronaries, the intestines, or the renal cortex could benefit from 3D ULM to study reperfusion, nutrient transport, or glomerulli. With further improvement in matrix transducer and portable scanners, volumetric ULM has the potential to be a tool for the longitudinal study of the microvasculature of entire organs, along with its variations for physiological or functional studies.

V. CONCLUSION

We report volumetric ULM, a vascular super-resolution ultrasound imaging technique surpassing the classical resolution limit by a factor larger than 10. We used 3D ULM to fully image a trepanned rat brain in vivo, successfully captured the entire cerebral vasculature, and co-registered it with a Waxholm space-based atlas. In each artery and vein depicted, we could derive blood velocity by calculating the velocity of ultrasound contrast agents circulating in each voxel. This enabled us to map hemodynamic vessel parameters in 3D. We foresee many applications for this technique in the future

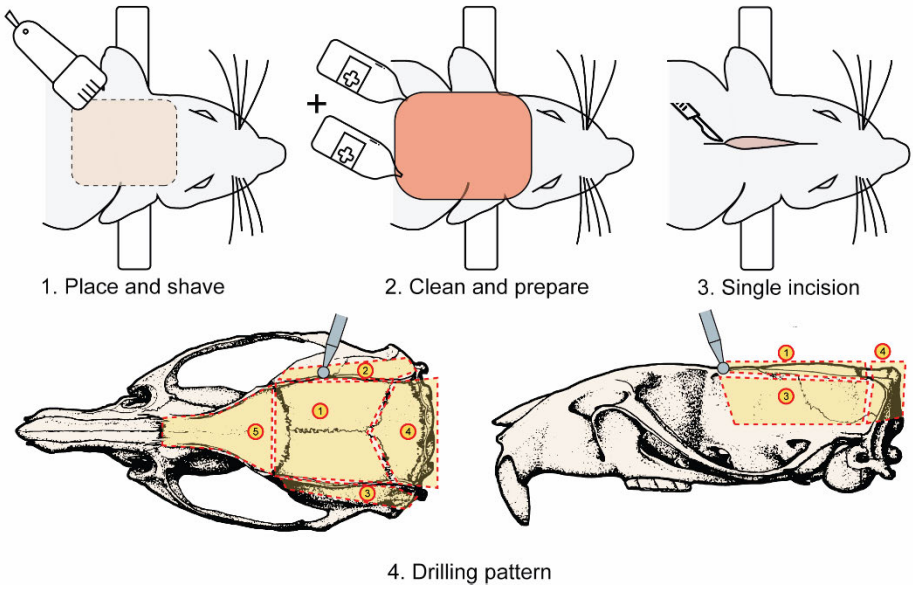

FIGURE 5. Steps to remove the whole skull from the brain: After the jugular vein catheter procedure, the rat is placed in the stereotactic frame using ear bars. A large zone of fur is trimmed (outlined with a dashed line). The skin on top of the skull is cleaned twice with 4% and 10% povidone-iodine solution An incision is made in the skin and the muscles are retracted from the skull. The surgery site is maintained open with suturing threads. Schematic of the drilling patterns (outlined with dashed line). Zone 1 is the biggest but the easiest to remove as the skull sutures are followed and drilling is made just below the side ridges where the skull is thinnest. Zone 4 just above the cerebellum is prone to bleeding as such it is done directly after zone 1. Then it is left to recover while drilling zone 5 over the olfactory bulb.

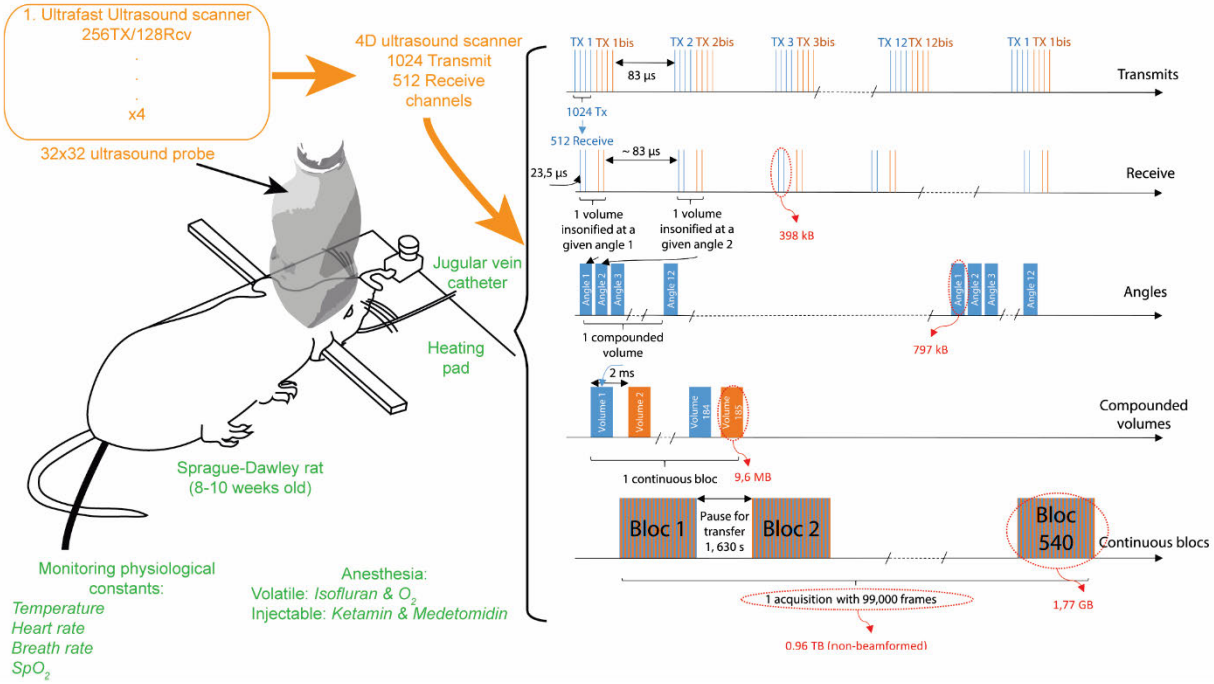

FIGURE 6. Setup and ultrasound sequence: The 32 × 32 fully populated matrix probe is connected through 4 connectors to a custom-built 4D ultrasound machine. This machine is capable of driving 1024 elements in transmit and has 512 receiving channels, meaning each transmit has to be doubled per receive. On the right of the graph, the transmit and receive pattern are drawn. The blue and orange pattern denote first and second set of transmit. We use 24 transmits to make up 12 angles for each volume. A compounded volume is repeated every 2 ms to reach 500Hz volume rate. To allow the data to be transferred to the hard drives, a block-to-block pattern is implemented with a pause in between each transfer of 1.630 s. The whole data for one single ULM volume weighs 0.96TB.

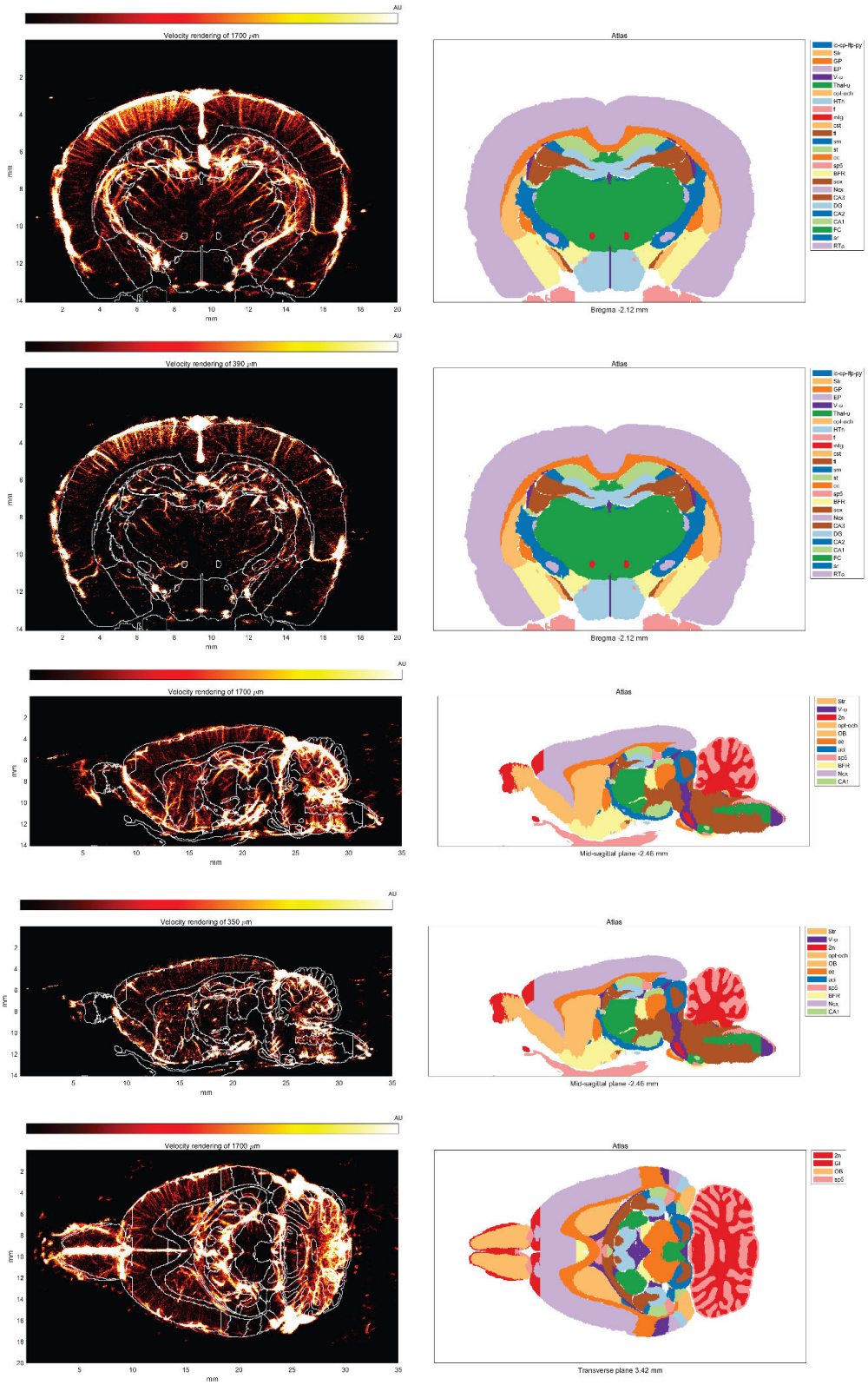

FIGURE 7. Volumetric ULM renderings registered with Waxholm-space atlas: Coronal, sagittal and transverse views of 2 slices with different thicknesses corresponding to $10\lambda = 1.7\ \mu m$ and $390\ \mu m$ which matches the size of 10 slices of the atlas used. ULM images are reconstructed from 7 ULM volumes stitched together and manually registered on Waxholm-space atlas. Abbreviations indicate functional areas as delimited in [14].

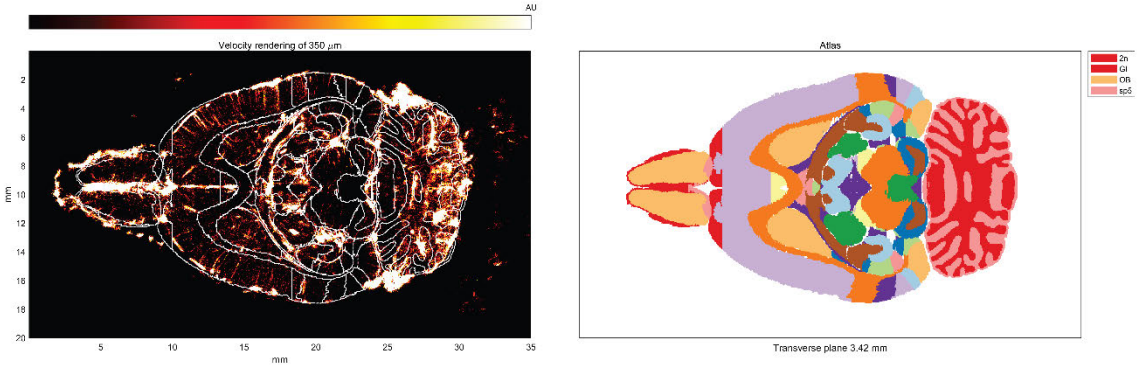

FIGURE 7. ***(Continued.)*** **Volumetric ULM renderings registered with Waxholm-space atlas: Coronal, sagittal and transverse views of 2 slices with different thicknesses corresponding to 10λ = 1.7 μm and 390 μm which matches the size of 10 slices of the atlas used. ULM images are reconstructed from 7 ULM volumes stitched together and manually registered on Waxholm-space atlas. Abbreviations indicate functional areas as delimited in [14].**

ranging from anatomical description of the vascular system to hemodynamics-based diagnosis of stroke, tumor microenvironments, or any deep investigation of microvascular function in opaque tissues.

APPENDIX

A. MATHEMATICAL DEMONSTRATION OF THE RADIAL SYMMETRY ALGORITHM IN 3D

The radial symmetry based localization algorithm is used for localization with an assumed full width at half maximum of 5 pixels in the three directions [11]. The positions of the microbubbles are then converted from pixels to micrometers. The mathematical demonstration of the algorithm will be developed here for one single microbubble:

The microbubble signal is set in a basis (z, x, y) similarily to the 2D case. We define the new basis (u, v, w) as:

$$(u, v, w) = \left(\begin{pmatrix} 1 \\ 1 \\ 1 \end{pmatrix}, \begin{pmatrix} -1 \\ 1 \\ -1 \end{pmatrix}, \begin{pmatrix} -1 \\ -1 \\ 1 \end{pmatrix} \right)_{(z,x,y)}$$

The rotation matrix from (z, x, y) to (u, v, w) is defined as:

$$R = \begin{bmatrix} & 1 & \\ 1 & 0 & 1+\sqrt{2} \\ 1+\sqrt{2} & 1 & 0 \\ 0 & 1+\sqrt{2} & 1 \end{bmatrix}$$

The cofactor matrix of R is calculated as:

$$Cof(R) = \begin{bmatrix} 1 & -(1+\sqrt{2}) & (1+\sqrt{2})^2 \\ (1+\sqrt{2})^2 & 1 & -(1+\sqrt{2}) \\ -(1+\sqrt{2}) & (1+\sqrt{2})^2 & 1 \end{bmatrix}$$

And as such the transpose is:

$$Cof(R)^T = \begin{bmatrix} 1 & (1+\sqrt{2})^2 & -(1+\sqrt{2}) \\ -(1+\sqrt{2}) & 1 & (1+\sqrt{2})^2 \\ (1+\sqrt{2})^2 & -(1+\sqrt{2}) & 1 \end{bmatrix}$$

The determinant is: $\det(R) = 8 + 5\sqrt{2}$.

The inverse of R is thus:

$$R^{-1} = \frac{1}{8+5\sqrt{2}} \begin{bmatrix} 1 & (1+\sqrt{2})^2 & -(1+\sqrt{2}) \\ -(1+\sqrt{2}) & 1 & (1+\sqrt{2})^2 \\ (1+\sqrt{2})^2 & -(1+\sqrt{2}) & 1 \end{bmatrix}$$

And it is the change of basis matrix from (u, v, w) to (z, x, y).

We define:

$$\begin{cases} dIdu = \dfrac{dI}{du} \\ dIdv = \dfrac{dI}{dv} \\ dIdw = \dfrac{dI}{dw} \end{cases}$$

As the differentiate of I with respect to (u, v, w) in the (u, v, w) basis. Their counterpart in the (z, x, y) basis are:

$$\begin{cases} dIdz = \dfrac{1}{8+5\sqrt{2}} \left(dIdu + (1+\sqrt{2})^2 dIdv - (1+\sqrt{2}) dIdw \right) \\ dIdx = \dfrac{1}{8+5\sqrt{2}} \left(dIdv + (1+\sqrt{2})^2 dIdw - (1+\sqrt{2}) dIdu \right) \\ dIdy = \dfrac{1}{8+5\sqrt{2}} \left(dIdw + (1+\sqrt{2})^2 dIdu - (1+\sqrt{2}) dIdv \right) \end{cases}$$

By applying the same reasoning as in the 2D case, we can calculate the distance from the initial guess of the center (z_c, x_c, y_c) to the vector u_d directed by the gradients in each pixel K:

$$d_K = \frac{\| KC \wedge u_d \|_{(z,x,y)}}{\| u_d \|_{(z,x,y)}}$$

And we define the weights as

$$w_K = \frac{\| u_d \|_{(u,v,w)}}{\| KC \|_{(z,x,y)}}$$

The notation $\| \|_{(z,x,y)}$, $\| \|_{(u,v,w)}$ defines in which basis the L2-norm is calculated.

TABLE 1. List of abbreviations of the anatomical areas defined by (Osen et al., 2019).

Abbreviation	Full name
Brain	Brain
wmt	White matter
cc	corpus callosum and associated subcortical white matter
ac	Anterior commissure
aca	anterior commissure, anterior part
acp	anterior commissure, posterior part
aci	anterior commissure, intrabulbar part
hiw	Hippocampal white matter
alv	alveus of the hippocampus
vhc	ventral hippocampal commissure
f	fornix
fi	fimbria of the hippocampus
cfp	Corticofugal pathways
ic-cp-lfp-py	descending corticofugal pathways
pyx	pyramidal decussation
ml	Medial lemniscus
ml	medial lemniscus
mlx	medial lemniscus decussation
tht	Thalamic tracts
mtg	mammillotegmental tract
cst	commissural stria terminalis
fr	fasciculus retroflexus
sm	stria medullaris of the thalamus
st	stria terminalis
hbc	habenular commissure
pc	posterior commissure
ar	auditory radiation
7n	Facial nerve
7n	facial nerve
asc7	ascending fibers of the facial nerve
g7	genu of the facial nerve
ofs	Optic fiber system and supraoptic decussation
2n	optic nerve
opt-och	optic tract and optic chiasm
sox	supraoptic decussation
tew	White matter of the tectum
csc	commissure of the superior colliculus
bsc	brachium of the superior colliculus
cic	inferior colliculus, commissure
bic	inferior colliculus, brachium
cbt	Cerebellar and precerebellar white matter
icp	inferior cerebellar peduncle
mcp	middle cerebellar peduncle
tfp	transverse fibers of the pons
bsw	White matter of the brainstem
ll	Lateral lemniscus
cll	lateral lemniscus, commissure
ll	lateral lemniscus
as	acoustic striae
tz	trapezoid body
sp5	spinal trigeminal tract
GM	Gray matter
CER	Cerebrum
Cx	Cerebral cortex
CPl	Cortical plate
Icx	Isocortex
Ncx	neocortex, unspecified
FrA	frontal association cortex
Cg	Cingulate cortex
Cg2	cingulate cortex, area 2
Au	Auditory cortex
Au1	primary auditory cortex
AuD	secondary auditory cortex, dorsal area
AuV	secondary auditory cortex, ventral area
OLF	Olfactory areas
GlA	glomerular layer of the accessory olfactory bulb
Gl	glomerular layer of the olfactory bulb
OB	olfactory bulb
HF	Hippocampal formation
FC	fasciola cinereum
SUB	subiculum
CA	Cornu Ammonis
CA1	cornu ammonis 1
CA2	cornu ammonis 2
CA3	cornu ammonis 3
DG	dentate gyrus
PHR	Parahippocampal region
POR	postrhinal cortex
PrS	presubiculum

TABLE 1. ***(Continued.)*** **List of abbreviations of the anatomical areas defined by (Osen et al., 2019).**

PaS	parasubiculum
PER	Perirhinal cortex
PER35	perirhinal area 35
PER36	perirhinal area 36
EC	Entorhinal cortex
MEC	medial entorhinal cortex
LEC	lateral entorhinal cortex
CSP	Cortical subplate
CNc	Cerebral nuclei
Str	striatum
PAL	Pallidum
GP	globus pallidus
EP	entopeduncular nucleus
SM	nucleus of the stria medullaris
ST	bed nucleus of the stria terminalis
Sep	septal region
BFR	basal forebrain region, unspecified
BS	Brainstem
BS-u	brainstem, unspecified
ItB	Interbrain
Thal	Thalamus
Thal-u	thalamus, unspecified
MG	Medial geniculate body
MGM	medial geniculate body, medial division
MGD	medial geniculate body, dorsal division
MGV	medial geniculate body, ventral division
MGMZ	medial geniculate body, marginal zone
RT	Reticular nucleus of the thalamus
RTa	reticular thalamic nucleus, auditory segment
Pi	pineal gland
HY	Hypothalamus
HTh	hypothalamic region
STh	subthalamic nucleus
MB	Midbrain
PT	pretectal region
Sag	nucleus sagulum
Tc	Tectum
IC	Inferior colliculus
DCIC	inferior colliculus, dorsal cortex
CNIC	inferior colliculus, central nucleus
ECIC	inferior colliculus, external cortex
Su	Superior colliculus
SuG	superficial gray layer of the superior colliculus

TABLE 1. ***(Continued.)*** **List of abbreviations of the anatomical areas defined by (Osen et al., 2019).**

SuD	deeper layers of the superior colliculus
Tg	Tegmentum
SN	substantia nigra
IP	interpeduncular nucleus
PAG	periaqueductal gray
HB	Hindbrain
P	Pons
Pn	pontine nuclei
MOb	Medulla oblongata
VCN	Cochlear nucleus, ventral part
AVCN	ventral cochlear nucleus, anterior part
PVCN	ventral cochlear nucleus, posterior part
Cap	ventral cochlear nucleus, cap area
GCL	ventral cochlear nucleus, granule cell layer
DCN	Cochlear nucleus, dorsal part
DCNM	dorsal cochlear nucleus, molecular layer
DCNFG	dorsal cochlear nucleus, fusiform and granule layer
DCND	dorsal cochlear nucleus, deep core
Sp5	spinal trigeminal nucleus
PVG	periventricular gray
SO	Superior olivary complex
NTB	nucleus of the trapezoid body
SPN	superior paraolivary nucleus
MSO	medial superior olive
LSO	lateral superior olive
SPR	superior periolivary region
VPO	ventral periolivary nucleus
LL	Nuclei of the lateral lemniscus
VLL	lateral lemniscus, ventral nucleus
ILL	lateral lemniscus, intermediate nucleus
DLL	lateral lemniscus, dorsal nucleus
IO	inferior olive
Cb	Cerebellum
MoCb	molecular cell layer of the cerebellum
DpCb	deeper cerebellum
V	Ventricular system
V-u	ventricular system, unspecified
4V	4th ventricle
CC	central canal
SpC	spinal cord
IE	Inner ear
VeA	vestibular apparatus
Co	cochlea
8cn	cochlear nerve
8vn	vestibular nerve
SpG	spiral ganglion

The goal of the radial symmetry based localization is to minimize the value of $\chi^2 = \sum_k d_k^2 w_k$, meaning we have to solve for

$$\begin{cases} \dfrac{d\chi^2}{dz_c} = 0(1) \\ \dfrac{d\chi^2}{dx_c} = 0\,(2) \\ \dfrac{d\chi^2}{dy_c} = 0(3) \end{cases}$$

$\frac{\partial d_k}{\partial z_c}, \frac{\partial d_k}{\partial x_c}, \frac{\partial d_k}{\partial y_c}$ were calculated and can be written as:

$$\begin{bmatrix} \dfrac{\partial d_k}{\partial z_c} \\ \dfrac{\partial d_k}{\partial x_c} \\ \dfrac{\partial d_k}{\partial y_c} \end{bmatrix} = \Omega_k \begin{bmatrix} z_k - z_c \\ x_k - x_c \\ y_k - y_c \end{bmatrix}$$

With $\Omega_k =$

$$\begin{bmatrix} -2(dIdx^2 + dIdy^2) & 2dIdxdIdz & 2dIdydIdz \\ 2dIdxdIdz & -2(dIdx^2 + dIdy^2) & 2dIdydIdx \\ 2dIdydIdz & 2dIdydIdx & -2(dIdx^2 + dIdy^2) \end{bmatrix}.$$

We can then write (1) , (2) , *and* (3)
As:
(1) $\Leftrightarrow \Sigma_k w_k\,(\Omega_{11} z_k + \Omega_{12} x_k + \Omega_{13} y_k) = (\Sigma_k w_k \Omega_{11}) z_c + (\Sigma_k w_k \Omega_{12}) x_c + (\Sigma_k w_k \Omega_{13}) y_c$
(2) $\Leftrightarrow \Sigma_k w_k\,(\Omega_{21} z_k + \Omega_{22} x_k + \Omega_{23} y_k) = (\Sigma_k w_k \Omega_{21}) z_c + (\Sigma_k w_k \Omega_{22}) x_c + (\Sigma_k w_k \Omega_{23}) y_c$
(3) $\Leftrightarrow \Sigma_k w_k\,(\Omega_{31} z_k + \Omega_{32} x_k + \Omega_{33} y_k) = (\Sigma_k w_k \Omega_{31}) z_c + (\Sigma_k w_k \Omega_{32}) x_c + (\Sigma_k w_k \Omega_{33}) y_c$.
If we write these equations in the matrix form, we have:

$$\begin{bmatrix} \Sigma_k w_k\,(\Omega_{11} z_k + \Omega_{12} x_k + \Omega_{13} y_k) \\ \Sigma_k w_k\,(\Omega_{21} z_k + \Omega_{22} x_k + \Omega_{23} y_k) \\ \Sigma_k w_k\,(\Omega_{31} z_k + \Omega_{32} x_k + \Omega_{33} y_k) \end{bmatrix}$$

$$= \begin{bmatrix} (\Sigma_k w_k \Omega_{11}) & (\Sigma_k w_k \Omega_{12}) & (\Sigma_k w_k \Omega_{13}) \\ (\Sigma_k w_k \Omega_{21}) & (\Sigma_k w_k \Omega_{22}) & (\Sigma_k w_k \Omega_{23}) \\ (\Sigma_k w_k \Omega_{31}) & (\Sigma_k w_k \Omega_{32}) & (\Sigma_k w_k \Omega_{33}) \end{bmatrix} \begin{bmatrix} z_c \\ x_c \\ y_c \end{bmatrix}$$

$$= M \begin{bmatrix} z_c \\ x_c \\ y_c \end{bmatrix}$$

We now have to invert M

The determinant of M is expressed as

$$\begin{aligned} &\det(M) \\ &= (\Sigma_k w_k \Omega_{11}) \left[(\Sigma_k w_k \Omega_{22})(\Sigma_k w_k \Omega_{33}) - (\Sigma_k w_k \Omega_{23})^2 \right] \\ &\quad - (\Sigma_k w_k \Omega_{12}) \left[(\Sigma_k w_k \Omega_{12})(\Sigma_k w_k \Omega_{33}) \right. \\ &\quad \left. - (\Sigma_k w_k \Omega_{13})(\Sigma_k w_k \Omega_{23}) \right] \\ &\quad + (\Sigma_k w_k \Omega_{13}) \left[(\Sigma_k w_k \Omega_{12})(\Sigma_k w_k \Omega_{23}) \right. \\ &\quad \left. - (\Sigma_k w_k \Omega_{13})(\Sigma_k w_k \Omega_{22}) \right] \end{aligned}$$

Which can also be rewritten as

$$\det(M) = (\Sigma_k w_k \Omega_{11})\alpha - (\Sigma_k w_k \Omega_{12})\beta + (\Sigma_k w_k \Omega_{13})\gamma$$

If we write

$$\delta = (\Sigma_k w_k \Omega_{11})(\Sigma_k w_k \Omega_{33}) - (\Sigma_k w_k \Omega_{13})^2$$

$$\phi = (\Sigma_k w_k \Omega_{11})(\Sigma_k w_k \Omega_{22}) - (\Sigma_k w_k \Omega_{12})^2$$

$$\epsilon = (\Sigma_k w_k \Omega_{11})(\Sigma_k w_k \Omega_{23}) - (\Sigma_k w_k \Omega_{13})(\Sigma_k w_k \Omega_{12})$$

Then we can calculate M^{-1} :

$$M^{-1} = \frac{1}{\det(M)} \begin{bmatrix} \alpha & -\beta & \gamma \\ -\beta & \delta & -\epsilon \\ \gamma & -\epsilon & \phi \end{bmatrix}$$

And thus finally we obtain (z_c, x_c, y_c):

$$\begin{pmatrix} z_c \\ x_c \\ y_c \end{pmatrix} = M^{-1} \begin{bmatrix} \Sigma_k w_k\,(\Omega_{11} z_k + \Omega_{12} x_k + \Omega_{13} y_k) \\ \Sigma_k w_k\,(\Omega_{21} z_k + \Omega_{22} x_k + \Omega_{23} y_k) \\ \Sigma_k w_k\,(\Omega_{31} z_k + \Omega_{32} x_k + \Omega_{33} y_k) \end{bmatrix}.$$

This triplet is calculated for each assumed microbubble signal and organized as a list to then go through the tracking algorithm.

B. SUPPLEMENTARY FIGURES

See Figures 5–7.

C. SUPPLEMENTARY TABLE

See Table 1.

REFERENCES

[1] E. Macé, G. Montaldo, I. Cohen, M. Baulac, M. Fink, and M. Tanter, "Functional ultrasound imaging of the brain," *Nature Methods*, vol. 8, pp. 662–664, May 2011, doi: 10.1038/nmeth.1641.
[2] D. B. Erlichman, A. Weiss, M. Koenigsberg, and M. W. Stein, "Contrast enhanced ultrasound: A review of radiology applications," *Clin. Imag.*, vol. 60, no. 2, pp. 209–215, Apr. 2020, doi: 10.1016/j.clinimag.2019.12.013.
[3] D. S. Richardson and J. W. Lichtman, "Clarifying tissue clearing," *Cell*, vol. 162, no. 2, pp. 246–257, 2015, doi: 10.1016/j.cell.2015.06.067.
[4] N. Renier, Z. Wu, D. J. Simon, J. Yang, P. Ariel, and M. Tessier-Lavigne, "IDISCO: A simple, rapid method to immunolabel large tissue samples for volume imaging," *Cell*, vol. 159, no. 4, pp. 896–910, Nov. 2014, doi: 10.1016/j.cell.2014.10.010.

[5] N. Renier et al., "Mapping of brain activity by automated volume analysis of immediate early genes," *Cell*, vol. 165, no. 7, pp. 1789–1802, Jun. 2016, doi: 10.1016/j.cell.2016.05.007.

[6] C. Kirst et al., "Mapping the fine-scale organization and plasticity of the brain vasculature," *Cell*, vol. 180, no. 4, pp. 780–795.e25, Feb. 2020, doi: 10.1016/j.cell.2020.01.028.

[7] M. I. Todorov et al., "Machine learning analysis of whole mouse brain vasculature," *Nature Methods*, vol. 17, no. 4, pp. 442–449, Apr. 2020, doi: 10.1038/s41592-020-0792-1.

[8] B. Xiong et al., "Precise cerebral vascular atlas in stereotaxic coordinates of whole mouse brain," *Frontiers Neuroanatomy*, vol. 11, p. 128, Dec. 2017, doi: 10.3389/fnana.2017.00128.

[9] B. P. Chugh et al., "Measurement of cerebral blood volume in mouse brain regions using micro-computed tomography," *NeuroImage*, vol. 47, no. 4, pp. 1312–1318, Oct. 2009, doi: 10.1016/j.neuroimage.2009.03.083.

[10] F. Helmchen, M. S. Fee, D. W. Tank, and W. Denk, "A miniature head-mounted two-photon microscope: High-resolution brain imaging in freely moving animals," *Neuron*, vol. 31, no. 6, pp. 903–912, 2001, doi: 10.1016/S0896-6273(01)00421-4.

[11] W. Denk, J. H. Strickler, and W. W. Webb, "Two-photon laser scanning fluorescence microscopy," *Science*, vol. 248, no. 4951, pp. 73–76, Apr. 1990, doi: 10.1126/science.2321027.

[12] A. Sigler and T. H. Murphy, "In vivo 2-Photon imaging of fine structure in the rodent brain: Before, during, and after stroke," *Stroke*, vol. 41, no. 10, pp. S117–S123, Oct. 2010, doi: 10.1161/STROKEAHA.110.594648.

[13] L. V. Wang, "Multiscale photoacoustic microscopy and computed tomography," *Nature Photon.*, vol. 3, no. 9, pp. 503–509, Sep. 2009, doi: 10.1038/nphoton.2009.157.

[14] H. F. Zhang, K. Maslov, G. Stoica, and L. V. Wang, "Functional photoacoustic microscopy for high-resolution and noninvasive in vivo imaging," *Nature Biotechnol.*, vol. 24, no. 7, pp. 848–851, Jul. 2006, doi: 10.1038/nbt1220.

[15] E. Betzig et al., "Imaging intracellular fluorescent proteins at nanometer resolution," *Science*, vol. 313, no. 5793, pp. 1642–1645, 2006, doi: 10.1126/science.1127344.

[16] O. Couture, B. Besson, G. Montaldo, M. Fink, and M. Tanter, "Microbubble ultrasound super-localization imaging (MUSLI)," in *Proc. IEEE Int. Ultrason. Symp.*, Oct. 2011, pp. 1285–1287, doi: 10.1109/ULTSYM.2011.6293576.

[17] K. Christensen-Jeffries et al., "Super-resolution ultrasound imaging," *Ultrasound Med. Biol.*, vol. 46, no. 4, pp. 865–891, 2020, doi: 10.1016/j.ultrasmedbio.2019.11.013.

[18] O. Couture, M. Tanter, and M. Fink, *Method and Device for Sound Imaging Patent 889 Cooperation Treaty (PCT)/FR2011/052810*, document FR1060633A, 2011.

[19] Y. Desailly, J. Pierre, O. Couture, and M. Tanter, "Resolution limits of ultrafast ultrasound localization microscopy," *Phys. Med. Biol.*, vol. 60, no. 22, pp. 8723–8740, Nov. 2015, doi: 10.1088/0031-9155/60/22/8723.

[20] C. Errico et al., "Ultrafast ultrasound localization microscopy for deep super-resolution vascular imaging," *Nature*, vol. 527, no. 7579, pp. 499–502, Nov. 2015, doi: 10.1038/nature16066.

[21] C. Demené et al., "Transcranial ultrafast ultrasound localization microscopy of brain vasculature in patients," *Nature Biomed. Eng.*, vol. 5, no. 3, pp. 219–228, Mar. 2021, doi: 10.1038/s41551-021-00697-x.

[22] J. Foiret, H. Zhang, T. Ilovitsh, L. Mahakian, S. Tam, and K. W. Ferrara, "Ultrasound localization microscopy to image and assess microvasculature in a rat kidney," *Sci. Rep.*, vol. 7, no. 1, Dec. 2017, Art. no. 13662, doi: 10.1038/s41598-017-13676-7.

[23] F. Lin, S. E. Shelton, D. EspíNdola, J. D. Rojas, G. Pinton, and P. A. Dayton, "3-D ultrasound localization microscopy for identifying microvascular morphology features of tumor angiogenesis at a resolution beyond the diffraction limit of conventional ultrasound," *Theranostics*, vol. 7, no. 1, pp. 196–204, 2017, doi: 10.7150/thno.16899.

[24] M. R. Lowerison, C. Huang, F. Lucien, S. Chen, and P. Song, "Ultrasound localization microscopy of renal tumor xenografts in chicken embryo is correlated to hypoxia," *Sci. Rep.*, vol. 10, no. 1, p. 2478, Dec. 2020, doi: 10.1038/s41598-020-59338-z.

[25] M. Siepmann, G. Schmitz, J. Bzyl, M. Palmowski, and F. Kiessling, "Imaging tumor vascularity by tracing single microbubbles," in *Proc. IEEE Int. Ultrason. Symp.*, Oct. 2011, pp. 1906–1909, doi: 10.1109/ULTSYM.2011.0476.

[26] T. Opacic et al., "Motion model ultrasound localization microscopy for preclinical and clinical multiparametric tumor characterization," *Nature Commun.*, vol. 9, no. 1, p. 1527, 2018, doi: 10.1038/s41467-018-03973-8.

[27] A. Chavignon, B. Heiles, V. Hingot, C. Orset, D. Vivien, and O. Couture, "3D transcranial ultrasound localization microscopy in the rat brain with a multiplexed matrix probe," *IEEE Trans. Biomed. Eng.*, vol. 69, no. 7, pp. 2132–2142, Jul. 2022, doi: 10.1109/TBME.2021.3137265.

[28] O. Demeulenaere et al., "In vivo whole brain microvascular imaging in mice using transcranial 3D ultrasound localization microscopy," *eBioMedicine*, vol. 79, May 2022, Art. no. 103995, doi: 10.1016/j.ebiom.2022.103995.

[29] B. Heiles, M. Correia, V. Hingot, M. Pernot, J. Provost, and O. Couture, "Ultrafast 3D ultrasound localization microscopy using a 32×32 matrix array," *IEEE Trans. Med. Imag.*, vol. 38, no. 9, pp. 2005–2015, Sep. 2019.

[30] V. Hingot, C. Errico, B. Heiles, L. Rahal, M. Tanter, and O. Couture, "Microvascular flow dictates the compromise between spatial resolution and acquisition time in ultrasound localization microscopy," *Sci. Rep.*, vol. 9, no. 1, p. 2456, 2019, doi: 10.1038/s41598-018-38349-x.

[31] G. Montaldo, M. Tanter, J. Bercoff, N. Benech, and M. Fink, "Coherent plane-wave compounding for very high frame rate ultrasonography and transient elastography," *IEEE Trans. Ultrason., Ferroelectr., Freq. Control*, vol. 56, no. 3, pp. 489–506, Mar. 2009, doi: 10.1109/TUFFC.2009.1067.

[32] C. Demené et al., "Spatiotemporal clutter filtering of ultrafast ultrasound data highly increases Doppler and fUltrasound sensitivity," *IEEE Trans. Med. Imag.*, vol. 34, no. 11, pp. 2271–2285, Nov. 2015, doi: 10.1109/TMI.2015.2428634.

[33] Y. Desailly, A.-M. Tissier, J.-M. Correas, F. Wintzenrieth, M. Tanter, and O. Couture, "Contrast enhanced ultrasound by real-time spatiotemporal filtering of ultrafast images," *Phys. Med. Biol.*, vol. 62, no. 1, pp. 31–42, 2017, doi: 10.1088/1361-6560/62/1/31.

[34] B. Heiles, A. Chavignon, V. Hingot, P. Lopez, E. Teston, and O. Couture, "Performance benchmarking of microbubble-localization algorithms for ultrasound localization microscopy," *Nature Biomed. Eng.*, vol. 6, no. 5, pp. 605–616, May 2022.

[35] E. Garyfallidis, M. Brett, M. M. Correia, G. B. Williams, and I. Nimmo-Smith, "QuickBundles, a method for tractography simplification," *Frontiers Neurosci.*, vol. 6, p. 13, Dec. 2012.

[36] E. A. Papp, T. B. Leergaard, E. Calabrese, G. A. Johnson, and J. G. Bjaalie, "Waxholm space atlas of the sprague dawley rat brain," *NeuroImage*, vol. 97, pp. 374–386, Aug. 2014, doi: 10.1016/j.neuroimage.2014.04.001.

[37] X. Benyi et al., "Precise cerebral vascular atlas in stereotaxic coordinates of whole mouse brain," *Frontiers Neuroanatomy*, vol. 11, 2017, doi: 10.3389/fnana.2017.00128.

[38] M. Sergejeva et al., "Anatomical landmarks for registration of experimental image data to volumetric rodent brain atlasing templates," *J. Neurosci. Methods*, vol. 240, pp. 161–169, Jan. 2015, doi: 10.1016/j.jneumeth.2014.11.005.

[39] L. J. Kjonigsen, S. Lillehaug, J. G. Bjaalie, M. P. Witter, and T. B. Leergaard, "Waxholm space atlas of the rat brain hippocampal region: Three-dimensional delineations based on magnetic resonance and diffusion tensor imaging," *NeuroImage*, vol. 108, pp. 441–449, Mar. 2015, doi: 10.1016/j.neuroimage.2014.12.080.

[40] K. K. Osen, J. Imad, A. E. Wennberg, E. A. Papp, and T. B. Leergaard, "Waxholm space atlas of the rat brain auditory system: Three-dimensional delineations based on structural and diffusion tensor magnetic resonance imaging," *NeuroImage*, vol. 199, pp. 38–56, Oct. 2019, doi: 10.1016/j.neuroimage.2019.05.016.

[41] J. Claron et al., "Large-scale functional ultrasound imaging of the spinal cord reveals in-depth spatiotemporal responses of spinal nociceptive circuits in both normal and inflammatory states," *Pain*, vol. 162, no. 4, pp. 1047–1059, Apr. 2021, doi: 10.1097/j.pain.0000000000002078.

[42] M. van Heel and M. Schatz, "Fourier shell correlation threshold criteria," *J. Struct. Biol.*, vol. 151, no. 3, pp. 250–262, Sep. 2005, doi: 10.1016/j.jsb.2005.05.009.

[43] R. P. J. Nieuwenhuizen, S. Stallinga, and B. Rieger, "Image resolution in optical nanoscopy," *Proc. SPIE*, vol. 8815, Sep. 2013, Art. no. 881508, doi: 10.1117/12.2025352.

[44] E. V. Orlova, P. Dube, J. R. Harris, E. Beckman, and F. Zemlin, "Structure of keyhole limpet hemocyanin type 1 (KLH1) at 15 a resolution by electron cryomicroscopy and angular reconstitution," *J. Mol. Biol.*, vol. 271, pp. 417–437, 1997.

[45] S. Zhai, A. Tanimura, S. M. Graves, W. Shen, and D. J. Surmeier, "Striatal synapses, circuits, and Parkinson's disease," *Current Opinion Neurobiol.*, vol. 48, pp. 9–16, Feb. 2018, doi: 10.1016/j.conb.2017.08.004.

[46] T. Sorimachi et al., "The striate artery, hematoma, and spot sign on coronal images of computed tomography angiography in putaminal intracerebral hemorrhage," *Stroke*, vol. 44, no. 7, pp. 1830–1832, Jul. 2013, doi: 10.1161/STROKEAHA.113.001498.

[47] L. M. Yager, A. F. Garcia, A. M. Wunsch, and S. M. Ferguson, "The ins and outs of the striatum: Role in drug addiction," *Neuroscience*, vol. 301, pp. 529–541, Aug. 2015, doi: 10.1016/j.neuroscience.2015.06.033.

[48] G. K. Rieke, D. E. Bowers, and P. Penn, "Vascular supply pattern to rat caudatoputamen and Globus pallidus: Scanning electronmicroscopic study of vascular endocasts of stroke-prone vessels," *Stroke*, vol. 12, no. 6, pp. 840–847, Nov. 1981, doi: 10.1161/01.STR.12.6.840.

[49] J. Sauvage et al., "4D functional imaging of the rat brain using a large aperture row-column array," *IEEE Trans. Med. Imag.*, vol. 39, no. 6, pp. 1884–1893, Jun. 2020, doi: 10.1109/TMI.2019.2959833.

[50] A. Bertolo, J. Sauvage, M. Tanter, M. Pernot, and T. Deffieux, "XDoppler: Cross-correlation of orthogonal apertures for 3D blood flow imaging," *IEEE Trans. Med. Imag.*, vol. 40, no. 12, pp. 3358–3368, Dec. 2021, doi: 10.1109/TMI.2021.3084865.

[51] C. Huang et al., "Short acquisition time super-resolution ultrasound microvessel imaging via microbubble separation," *Sci. Rep.*, vol. 10, no. 1, p. 6007, Dec. 2020, doi: 10.1038/s41598-020-62898-9.

[52] T. M. Kierski et al., "Superharmonic ultrasound for motion-independent localization microscopy: Applications to microvascular imaging from low to high flow rates," *IEEE Trans. Ultrason., Ferroelectr., Freq. Control*, vol. 67, no. 5, pp. 957–967, May 2020, doi: 10.1109/TUFFC.2020.2965767.

[53] C. Brunner and Grillet, "A platform for brain-wide functional ultrasound imaging and analysis of circuit dynamics in behaving mice," *Neuron*, vol. 108, no. 5, p. 29, Dec. 2020.

[54] D. E. Soulioti, D. Espíndola, P. A. Dayton, and G. Pinton, "Super resolution imaging through the human skull," 2018, *arXiv:1811.10653*.

[55] V. Hingot et al., "Early ultrafast ultrasound imaging of cerebral perfusion correlates with ischemic stroke outcomes and responses to treatment in mice," *Theranostics*, vol. 10, no. 17, pp. 7480–7491, 2020, doi: 10.7150/thno.44233.

[56] P. Guevara et al., "Robust clustering of massive tractography datasets," *NeuroImage*, vol. 54, no. 3, pp. 1975–1993, Feb. 2011, doi: 10.1016/j.neuroimage.2010.10.028.

[57] A. Vázquez et al., "FFClust: Fast fiber clustering for large tractography datasets for a detailed study of brain connectivity," *NeuroImage*, vol. 220, Oct. 2020, Art. no. 117070, doi: 10.1016/j.neuroimage.2020.117070.

[58] B. Heiles, D. Terwiel, and D. Maresca, "The advent of biomolecular ultrasound imaging," *Neuroscience*, vol. 474, pp. 122–133, Oct. 2021, doi: 10.1016/j.neuroscience.2021.03.011.

[59] M. G. Shapiro et al., "Biogenic gas nanostructures as ultrasonic molecular reporters," *Nature Nanotechnol.*, vol. 9, no. 4, pp. 311–316, Apr. 2014, doi: 10.1038/nnano.2014.32.

[60] N. Hamano et al., "Development of antibody-modified nanobubbles using Fc-region-binding polypeptides for ultrasound imaging," *Pharmaceutics*, vol. 11, no. 6, p. 283, Jun. 2019, doi: 10.3390/pharmaceutics11060283.

[61] Y. Gao et al., "Ultrasound molecular imaging of ovarian cancer with CA-125 targeted nanobubble contrast agents," *NanoMed., Nanotechnol., Biol. Med.*, vol. 13, no. 7, pp. 2159–2168, Oct. 2017, doi: 10.1016/j.nano.2017.06.001.

[62] A. Farhadi, G. H. Ho, D. P. Sawyer, R. W. Bourdeau, and M. G. Shapiro, "Ultrasound imaging of gene expression in mammalian cells," *Science*, vol. 365, no. 6460, pp. 1469–1475, Sep. 2019.

[63] R. Gao et al., "Cortical column and whole-brain imaging with molecular contrast and nanoscale resolution," *Science*, vol. 363, no. 6424, Jan. 2019, Art. no. eaau8302, doi: 10.1126/science.aau8302.

[64] J. Provost, C. Papadacci, C. Demene, J.-L. Gennisson, M. Tanter, and M. Pernot, "3-D ultrafast Doppler imaging applied to the noninvasive mapping of blood vessels in vivo," *IEEE Trans. Ultrason., Ferroelectr., Freq. Control*, vol. 62, no. 8, pp. 1467–1472, Aug. 2015.

[65] R. Parthasarathy, "Rapid, accurate particle tracking by calculation of radial symmetry centers," *Nature Methods*, vol. 9, no. 7, pp. 724–726, Jul. 2012, doi: 10.1038/nmeth.2071.

[66] J. M. Soares, P. Marques, V. Alves, and N. Sousa, "A hitchhiker's guide to diffusion tensor imaging," *Frontiers Neurosci.*, vol. 7, p. 31, Mar. 2013, doi: 10.3389/fnins.2013.00031.

[67] W. Luo, J. Xing, A. Milan, X. Zhang, W. Liu, and T.-K. Kim, "Multiple object tracking: A literature review," 2014, *arXiv:1409.7618*.